Non-linear spacing policy and network analysis for shared-road platooning

Final Report

Michael Levin
Rejesh Rajamani
Woongsun Jeon
Rongshen Chen
Di Kang

Department of Civil, Environmental,
and Geo- Engineering
University of Minnesota

CTS 19-27

Technical Report Documentation Page

1. Report No.	2.	3. Recipients Accession No.
CTS 19-27		

4. Title and Subtitle	5. Report Date
Non-linear spacing policy and network analysis for shared-road platooning	August 2019
	6.

7. Author(s)	8. Performing Organization Report No.
Michael W. Levin, Rajesh Rajamani, Woongsun Jeon, Rongsheng Chen, Di Kang	

9. Performing Organization Name and Address	10. Project/Task/Work Unit No.
Department of Civil, Environmental, and Geo-Engineering Department of Mechanical Engineering University of Minnesota	CTS Project# 2018075
	11. Contract (C) or Grant (G) No.

12. Sponsoring Organization Name and Address	13. Type of Report and Period Covered
Center for Transportation Studies University of Minnesota University Office Plaza, Suite 440 2221 University Ave SE Minneapolis, MN 55414	Final Report
	14. Sponsoring Agency Code

15. Supplementary Notes

http://www.cts.umn.edu/Publications/ResearchReports/

16. Abstract (Limit: 250 words)

Connected vehicle technology creates new opportunities for obtaining knowledge about the surrounding traffic and using that knowledge to optimize individual vehicle behaviors. This project creates an interdisciplinary group to study vehicle connectivity, and this report discusses three activities of this group. First, we study the problem of traffic state (flows and densities) using position reports from connected vehicles. Even if the market penetration of connected vehicles is limited, speed information can be inverted through the flow-density relationship to estimate space- and time-specific flows and densities. Propagation, according to the kinematic wave theory, is combined with measurements through Kalman filtering. Second, the team studies the problem of cyber-attack communications. Malicious actors could hack the communications to incorrectly report position, speed, or accelerations to induce a collision. By comparing the communications with radar data, the project team develops an analytical method for vehicles using cooperative adaptive cruise control to detect erroneous or malicious data and respond accordingly (by not relying on connectivity for safe following distances). Third, the team considers new spacing policies for cooperative adaptive cruise control and how they would affect city traffic. Due to the computational complexity of microsimulation, the team elects to convert the new spacing policy into a flow-density relationship. A link transmission model is constructed by creating a piecewise linear approximation. Results from dynamic traffic assignment on a city network shows that improvements in capacity reduces delays on freeways, but surprisingly route choice increased congestion for the overall city.

17. Document Analysis/Descriptors	18. Availability Statement
Traffic platooning, Kalman filtering, Traffic estimation, Mobile communication systems, Traffic density, Traffic flow, Connected vehicles, Data analysis, Data collection	No restrictions. Document available from: National Technical Information Services, Alexandria, Virginia 22312

19. Security Class (this report)	20. Security Class (this page)	21. No. of Pages	22. Price
Unclassified	Unclassified	68	

Non-linear spacing policy and network analysis for shared-road platooning

FINAL REPORT

prepared by:

Michael W. Levin, Ph.D.
Rongsheng Chen
Di Kang
Department of Civil, Environmental, and Geo- Engineering
University of Minnesota

Rajesh Rajamani, Ph.D.
Woongsun Jeon
Department of Mechanical Engineering
University of Minnesota

August 2019

Published by:

Center for Transportation Studies
University of Minnesota
University Office Plaza, Suite 440
2221 University Ave SE
Minneapolis, MN 55414

Acknowledgements

The funding for this project was provided by the Center for Transportation Studies.

Contents

List of Figures

List of Tables

Chapter 1

Introduction

This CTS Scholar Seed grant brought together two researchers from different disciplines to study adaptive cruise control and its effects on traffic flow. Dr. Rajamani studied spacing policies and car-following control using connected vehicle data. Dr. Levin integrated the novel car-following behaviors into a traffic model that was implemented in simulation to study the effects on city network traffic congestion.

The project proposal planned an in-depth study of a new spacing policy based on the safe car-following available from platooning. This spacing policy, constructed by Dr. Rajamani, would be converted into a speed-density relationship in steady (zero acceleration) conditions. The resulting flow-density relationship would be implemented in a kinematic wave theory, solved using a numerical approximation, and studied in dynamic traffic assignment. These results are indeed included in Chapter 4. However, as part of the objective to create synergistic activities between the two disciplines, the project scope was expanded to a range of sensor-based traffic flow work. In addition to the original project scope, the project team also jointly studied the traffic state and vehicle trajectory estimation problem using basic safety messages from connected vehicles. Also, cybersecurity of adaptive cruise control was addressed through methods of detecting malicious or otherwise incorrect transmitted position, speed, and acceleration data that could result in a collision.

This project has contributed to several papers that have been submitted or will soon be submitted to peer-reviewed conferences and journals.

- *Resilient control under cyber-attacks and sensor health monitoring in connected ACC vehicles.* Safe car-following requires accurate information to ensure that speed and acceleration changes in the leading vehicle are matched by the acceleration of the following vehicle. This paper, submitted to the *Dynamic Systems and Control Conference*, studies the detection of erroneous and/or malicious (from cyberattacks) data that, if present, could cause a collision between vehicles using cooperative adaptive cruise control.

- *City network analysis of non-linear spacing policy for adaptive cruise control.* Cooperative adaptive cruise control (platooning) creates opportunities for new car-following behaviors than those currently used by drivers. In particular, higher speeds are safely

possible at high densities by coordination of vehicle accelerations. In this paper, which is planned for submission to *IEEE Transactions on Intelligent Transportation Systems*, we construct a kinematic wave theory of the car-following behavior using a novel flow-density relationship. The kinematic wave theory is numerically solved using the link transmission model, and by using it within dynamic traffic assignment we predict the effects of platooning on route choice and congestion on the Round Rock city network.

- *Traffic state estimation using basic safety messages from connected vehicles.* NHTSA has proposed that all new vehicles from 2021 will be required to broadcast basic safety messages with their position, speed, and acceleration information to improve collision avoidance. Such data, if received by roadside units, could be used to estimate the traffic state (the flow and density conditions that evolve over space and time). This paper, which will be submitted to *IEEE Transactions on Intelligent Transportation Systems*, used Kalman filtering to estimate both the flow-density relationship and the flow and density functions.

Using these results as preliminary work, the authors are in the process of writing an NSF proposal.

The remainder of this report is organized as follows. In Chapter 2, we discuss traffic state estimation based on connected vehicle data. Chapter 3 approaches a similar problem — the use of connected vehicle data for car-following in platooning, but with an emphasis on detecting and responding to erroneous or malicious transmissions. Chapter 4 connects platooning to dynamic traffic assignment by constructing a link transmission model for a novel platooning flow-density relationship and studying the interactions between route choice and congestion on a city network. In Chapter 5, we discuss conclusions and future directions for this work.

Chapter 2

Traffic State estimation from Basic Safety Messages

2.1 Introduction

Traffic information plays an important role in the operation of an intelligent traffic system. Traffic models need adequate information to calibrate their parameters so that the traffic management and control system can react to the variation in traffic conditions and maintain the efficiency of traffic networks. Traffic information is collected by traffic detectors, such as loop detectors and video detectors. These detectors are installed at specific locations and are hard to maintain. For example, the loop detector only collects data at specific locations and it needs to be embedded in the pavement. The video detector should be installed at high buildings. Its detection is greatly affected by the weather and light condition, and the processing of video image data requires a lot of time and storage. The accuracy of video data is also limited by the location of the cameras.

Basic safety message (BSM) data from equipped vehicles provides us the opportunity of extracting traffic information for the entire road without the limitation of the location and the installation of traffic detectors. This type of BSM data is similar to probe vehicle data, which is collected from moving vehicles equipped with data collection facilities. The on-vehicle detectors can provide basic information such as vehicle locations, speeds, and moving directions of vehicles.

This chapter is organized as follows. Section 2.1.1 includes studies about the traffic state estimation using the vehicle trajectory data and the Kalman filtering technique. Section 2.2 introduces the algorithm used to get the traffic state estimation, including the equations for the cell transmission model and the Kalman filter. Section 2.3 proposes the method used to calibrate the parameters of the fundamental diagram used in the cell transmission model. Section 2.4 shows the experiment that the research team conducted to test the accuracy of the proposed algorithm, including two tests using simulators based on the cell transmission model and a test using the microscopic simulation model. Section 2.5 lists the tasks that the research team is going to work on in the future.

2.1.1 Background

With the need for equipped vehicles, BSM data provides an incomplete picture.The research topic that uses incomplete information to estimate traffic state is called the traffic state estimation problem. The characteristic of this type of study is that the data the data only represents equipped vehicles instead of all vehicles. There are some existing studies related to the traffic state estimation problem using the probe vehicle technique or vehicle trajectory data.

Hellinga et al. (2008) estimated average link travel times with low-frequency anonymous taxi trajectory data. This travel time allocation problem was solved by a travel time decomposition method which was able to compute the congestion time and the stopping time on a link. The result showed that this method improved the accuracy of travel time estimation by 40% on average with a frequency of one-minute compared with the baseline method, which proportionally assigned the travel time on each link according to its free flow travel time.

Work et al. (2008) derived a velocity model based PDE on the Lighthill-Whitham-Richard PDE. A velocity cell transmission model (CTM-v) was built after integrating the new PDE with the derived velocity model. The Ensemble Kalman filtering (EnKF) technique was used to estimate the velocity based on the GPS data. The velocity estimation was validated with microsimulation data and historical velocity data and proven to have less error than the averaging scheme. In another study by Work et al., a traffic estimation system was built using GPS-equipped smartphone data and Virtual Trip Lines (VTLs) data. The result showed that the difference between the estimation of the system and the loop detector data, which served as the ground truth, was about 10% for the entire network.

Herring et al. (2010) utilized taxi trajectory data to estimate arterial traffic conditions. A fleet of 500 taxis was used to collect GPS data with a frequency of one minute. An expectation maximization algorithm was developed to estimate parameters in a Coupled Hidden Markov Model (CHMM). Then CHMM was used for the prediction of link travel time. The result showed that this model had a higher accuracy than the baseline model by 35%.

Zheng and Van Zuylen (2013) estimated the link travel time from low-frequency trajectory data using a three-layer ANN model. This model was evaluated with the simulation results in VISSIM. The results showed that the ANN model had a mean absolute percentage error lower than 6%.

Wang et al. (2013) extracted road speeds and traffic congestion events from the taxi trajectory data collected in Beijing. The data was cleaned and mapped to the road network. Based on road speed values, traffic congestion events were detected and categorized. A visualization tool was then developed to analyze the data by space, time, and topology.

Li et al. (2015) used cloud-based probe data from cell phone navigation applications to detect the boundary of congested and uncongested conditions. Differences in speeds of two adjacent segments were calculated and compared with predefined threshold values. Two adjacent road segments were regarded as high-risk segments if their speed difference was larger than the threshold value. This detection method was validated by comparing detected high-risk segments with images collected in Indiana. The results showed that this

method can effectively identify locations of vehicle queues.

Rahmani et al. (2015) proposed a travel time allocation model used to derive route travel times from low-frequency float car data. The method was tested using observed route travel times. The float car data had bias introduced by the incomplete and uneven coverage of the route. This paper recommended integrating multiple data resources to evaluate route travel times.

Rouphail et al. (2017) estimated the free flow speed using probe vehicle data. The data were collected by a fleet of 20 vehicles running on target road segments. Free flow speed was estimated by fitting a linear regression. This study also explored the effects of posted speed limits, driver familiarity, and section ramp density on the free flow density.

Yao et al. (2017) used the taxi trajectory data from taxis in Foshan, China to do short-term traffic speed prediction. The trajectory data were collected from a long arterial made up of six 4-lane road sections. Six models were applied for the 5-minute short-term prediction. The results showed that the support vector machine model with spatial-temporal parameters had a better prediction than all the other models with a mean average percentage of error lower than 16%.

Zhan et al. (2017) proposed a framework to predict the traffic volume. This framework included a method to derive the flow-speed relationship using trajectory data and the speed distribution on the road and a prediction model to regenerate the traffic volume. This prediction framework was tested using the taxi trajectory data and actual traffic volumes recorded by video clips. The results showed that this framework had higher accuracy for highways (with a mean relative error lower than 30%) but had lower accuracy for lower level roads (with a mean relative error higher than 50%).

There are some studies focused on developing Kalman filter algorithms to estimate traffic states. Sun et al. (2003) presented a vehicle density estimator using a mixture Kalman filtering algorithm on the switching-mode traffic model. Field collected data from a 14-mile long segment of Interstate Highway 210 was used to verify the model accuracy.

Wang et al. (2005, 2008) proposed a general approach to estimate the traffic state of a freeway in real-time based on an extended Kalman filter. A macroscopic traffic flow model was used as the prediction step in the Kalman filter while loop detector data supported the measurement step. Several simulations were conducted to test the model accuracy and the effect of parameter estimation on traffic state estimation. The study emphasized the importance of parameter estimation for accurate traffic state estimation and the model was sensitive to the initial values of the model parameters. The results showed that a well-designed traffic state estimator along with real-time model parameter estimation can produce estimation with high accuracy.

Zhu et al. (2009) proposed an algorithm to predict the travel times for urban arterial roads based on Kalman filtering using the float car data. The hierarchical clustering was used to estimate the parameters in the model. The results showed that the proposed algorithm could be applied to provide real-time travel time prediction services.

Wang et al. (2018) designed a parallel computing framework for traffic state estimation. In this framework, a genetic algorithm was used for model calibration, and an improved Kalman filter process was used to get the model estimation with traffic data. The results

showed that the proposed algorithm had some advantages over the traditional Kalman filter.

Most studies use loop detector data to serve as the measurement for occupancies and flow rates, which greatly decreases the difficulty for traffic state estimation because the measurements of flow rates and occupancies provided by loop detectors can cover all vehicles. There are few studies using probe vehicle data to estimate traffic states, but the algorithms in these studies focus on predicting only one traffic variable, such as the travel time or the travel speed.

2.2 Traffic State Estimation

In this section, a Kalman filter is used to estimate traffic states. Kalman filtering (Kalman, 1960) is an algorithm that integrates measurements and model-based predictions. Both of them contain errors and other uncertainties. The Kalman filter is able to generate an estimation that is more accurate than any of these single measurements or predictions. The Kalman filter iterates between the measurement step and the prediction step.

2.2.1 Cell Transmission model

In the prediction part, the cell transmission model is applied to model the dynamics of traffic flow. The cell transmission model (CTM) is a discretization of the Lighthill-Whitham-Richards partial differential equation (Lighthill and Whitham, 1955; Richards, 1956) using a Godunov scheme. The parameters in CTM are based on a fundamental diagram, such as triangular or trapezoidal diagrams. Figure 2.1 shows a triangular fundamental diagram of traffic flow q as a function of density k. It includes four parameters: the capacity Q, the free-flow speed v_f, the jam density K, and the backward shockwave speed w. In the cell transmission model with a time step size of Δt, the road section was divided into several cells with cell length $\Delta L = \Delta t \cdot v_f$. The cell occupancy for each cell can be updated using equation (2.1). The cell occupancy $n_i(t)$ mentioned in this report is not the percentage of time when a loop detector is occupied but represents the number of vehicles in a cell i at a

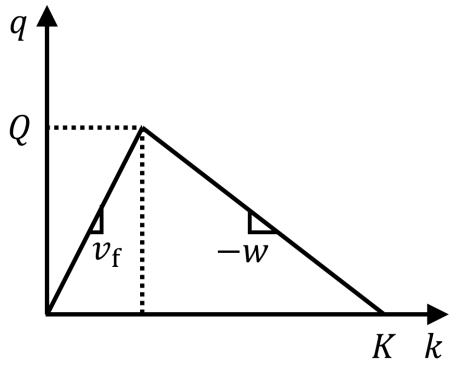

Figure 2.1: Trapezoidal fundamental diagram

time step t, which equals the product of density and the cell length. In equation (2.1), the occupancy n of cell i at time $t+1$ equals the occupancy of cell i at time t minus the exiting flow from the current cell, y_i, plus the entering flow from the previous cell, y_{i-1}.

$$n_i(t+1) = n_i(t) - y_i(t) + y_{i-1}(t) \tag{2.1}$$

Equation (2.2) shows how the inter-cell flow is calculated.

$$y_i(t) = \min\{n_i(t), Q\Delta t, \frac{w}{v_f}(N_{i+1} - n_{i+1}(t))\} \tag{2.2}$$

There are three terms in the minimization function of equation (2.2). The first term $n_i(t)$ is the occupancy of cell i at time t. The second term, $Q\Delta t$, is the product of the capacity and the time step size, which is the largest value of the inter-cell flow. The third term $\frac{w}{v_f}(N_{i+1} - n_i)$ includes the backward shockwave speed w, the free flow speed v_f, and the maximum occupancy N in cell $i+1$. The maximum occupancy N is calculated using the jam density K and the cell length ΔL, which is $N = K \times \Delta L$. The third term represents the available space in the next cell.

2.2.2 The Structure of the Kalman Filter

In the Kalman filter with CTM, BSM data including vehicle locations and speeds can be processed to obtain relevant traffic state information such as density, flow, and speed. The basic equations of the Kalman filter are shown in this section.

The prediction step in equation (2.5) is made up of the state vector $\mathbf{N}(t)$ and the control vector $\mathbf{Y}(t)$. The state vector includes the occupancies of all road segments. The reason why only the occupancy is included in the state vector is that other traffic state variables, such as the flow and the speed, can be calculated using the occupancy based on the fundamental diagram. The calculation of occupancies requires the knowledge of incoming flows and outgoing flows, which is included in control vector $\mathbf{Y}(t)$ in equation (2.4). The first element $y_0(t)$ is the input flow to the road, which is assumed to be the measured flow for equipped vehicle $y_0^p(t)$ divided by the penetration rate r.

$$\mathbf{N}(t) = \begin{bmatrix} n_1(t) \\ n_2(t) \\ \vdots \\ n_i(t) \end{bmatrix} \tag{2.3}$$

$$\mathbf{Y}(t) = \begin{bmatrix} y_0(t) \\ y_1(t) \\ \vdots \\ y_i(t) \end{bmatrix} \tag{2.4}$$

The relation between the state vector $\mathbf{N}(t)$ and the control vector $\mathbf{Y}(t)$ can be written as

the form in equation (2.5).

$$\mathbf{N}(t+1) = \mathbf{A_r}\mathbf{N}(t) + \mathbf{B_r}\mathbf{Y}(t+1) + \mathbf{Q_r}^* \tag{2.5}$$

In equation (2.5), the state vector at time $t+1$ is updated with the state vector at time t and the control vector at time $t+1$. $\mathbf{A_r}$ is an identity matrix. $\mathbf{B_r}$ is a matrix with i rows and $i+1$ columns with all elements equal to -1, 0 or 1. Its form is shown in equation (2.6). The matrices $\mathbf{A_r}$ and $\mathbf{B_r}$ are derived from the relation between the state vector and the control vector shown in equation (2.1). Matrix $\mathbf{Q_r}^*$ is the error term for the prediction.

$$\mathbf{B_r} = \begin{bmatrix} 1 & -1 & 0 & 0 & \dots & 0 & 0 \\ 0 & 1 & -1 & 0 & \dots & 0 & 0 \\ 0 & 0 & 1 & -1 & \dots & 0 & 0 \\ \vdots & \vdots & \vdots & \vdots & \ddots & \vdots & \vdots \\ 0 & 0 & 0 & 0 & \dots & 1 & -1 \end{bmatrix} \tag{2.6}$$

Equation (2.7) shows the measurement step of the Kalman Filter. $\hat{\mathbf{N}}(t)$ is the measurement of occupancies. $\mathbf{C_r}$ is an identity matrix. $\mathbf{R_r}$ is the error term related with measurement, such as measurement errors from detectors. In this study, the relation between the measured occupancy for all vehicles $\hat{\mathbf{N}}$ and the measured occupancies for equipped vehicles $\mathbf{N}_p$ can be represented by function $\mathbf{G}$.

$$\hat{\mathbf{N}}(t) = \mathbf{C_r}\mathbf{G}\left(\hat{\mathbf{N}}_p(t), \hat{\mathbf{V}}_p(t)\right) + \mathbf{R_r} \tag{2.7}$$

$$\mathbf{G}\left(\hat{\mathbf{N}}_p(t), \hat{\mathbf{V}}_p(t)\right) = \begin{cases} \frac{\hat{\mathbf{N}}_p(t)}{r}, & \hat{\mathbf{V}}_p(t) \geq 0.9 v_{\mathrm{f}} \\ \frac{wK\Delta l}{\hat{\mathbf{V}}_p(t)+w}, & \hat{\mathbf{V}}_p(t) < 0.9 v_{\mathrm{f}} \end{cases} \tag{2.8}$$

In equation (2.8), when the measured average speed of probe vehicles $\hat{\mathbf{V}}_p(t)$ is greater or equal to 0.9 times the free-flow speed, the traffic is considered uncongested. Then the measured occupancy is the measured number of equipped vehicles $\hat{\mathbf{N}}_p(t)$ divided by the assumed penetration rate r. Otherwise, the road is congested. The occupancy is calculated by finding the corresponding value on the fundamental diagram using the measured speed of equipped vehicles. If no speed data is available at the current time step, the measurement at the previous time step is used. To make the fundamental diagram accurately represent the dynamics of traffic flow on the road, the values of capacity Q, the free-flow speed v_{f}, and the jam density K should be calibrated in advance or updated in real-time. The parameter calibration will be discussed in section 4. The covariance matrix $\mathbf{P_r}$ can be updated using equation (2.9). As matrix $\mathbf{A_r}$ is a identity matrix, matrix $\mathbf{P_r}$ can be calculated by adding up matrix $\mathbf{A_r}$ and the covariance matrix $\mathbf{Q_r}^*$.

$$\mathbf{P_r}(t+1) = \mathbf{A_r}\mathbf{P_r}(t)\mathbf{A_r}^{\intercal} + \mathbf{Q_r}^* \tag{2.9}$$

The Kalman Gain $\mathbf{K_r}$, which serves as the weight of measurement over prediction in the

estimation, is calculated by equation (2.10).

$$\mathbf{K_r}(t+1) = \mathbf{P_r}(t+1|t)\mathbf{C_r}^\intercal \left[\mathbf{C_r}\mathbf{P_r}(t+1|t)\mathbf{C_r}^\intercal + \mathbf{R_r}\right]^{-1} \tag{2.10}$$

Using Kalman Gain $\mathbf{K_r}$, the values of predictions and measurements can be integrated and the covariance matrix $\mathbf{P_r}$ can be updated, as shown in equations (2.11) and (2.12).

$$\mathbf{N}(t+1|t+1) = \mathbf{N}(t+1|t) + \mathbf{K_r}(t+1)\left[\hat{\mathbf{N}}(t+1) - \mathbf{C_r}\mathbf{N}(t+1|t)\right] \tag{2.11}$$

$$\mathbf{P_r}(t+1|t+1) = \mathbf{P_r}(t+1|t) - \mathbf{K_r}(t+1)\mathbf{C_r}\mathbf{P_r}(t+1|t) \tag{2.12}$$

With the segment length ΔL, the occupancy can be converted to density $k_i(t) = n_i(t)/\Delta L$. With the value of k, the flow rate and speed can also be estimated.

2.3 Parameter Calibration

CTM relies on accurate fundamental diagram parameters, which vary depending on the road and the weather conditions. It is necessary to estimate parameters to make them reflect the traffic flow dynamics on the target road. These parameters include the capacity Q, the free-flow seed v_f, the backward shockwave speed w, and the jam density K. To simplify the process of parameter calibration, the value for the jam density K is first calculated by the average car length ℓ, as shown in (2.13). Then the parameter calibration will not update the value for the jam density.

$$K = \frac{1}{\ell} \tag{2.13}$$

2.3.1 Calibration Process

It is assumed that all road segments on a road with the same number of lanes share the same parameters in the fundamental diagram. The parameter calibration uses a lower frequency to update the values of parameters than the traffic state estimation process mentioned in section 2.2.

2.3.2 Measurement of Parameters

The values of the free-flow speed, the capacity, and the shockwave speed should be measured from the BSM data.

Free-flow speed

If the road is congested during the previous time step, and the average speed at the current time step is much larger than that in the previous time step, then the current average speed, $\bar{v}(t)$, will be used as the new estimation of the free-flow speed. For BSM data, it is hard to directly get measurements of the capacity and the shockwave speed because BSM data only

includes the occupancy and flow related to equipped vehicles. However, it is assumed that the average speed of equipped vehicles can represent the speed for the entire road segment in the road section. If there is no huge drop in the measured capacity, the free-flow speed can be extracted by getting the larger value between the average speed at the current time and the value of free-flow speed at the previous time step, as shown in equation (2.14). If a drop in the measured capacity is observed, the measured value for free-flow speed can be decreased, as shown in equation (2.15).

$$\hat{v}_{\mathrm{f}}(t) = \max\left(\hat{v}_{\mathrm{f}}(t-1), \bar{v}(t)\right) \tag{2.14}$$

$$\hat{v}_{\mathrm{f}}(t) = \bar{v}(t) \tag{2.15}$$

Capacity and the backward shockwave speed

In the triangular fundamental diagram, the traffic has congested and uncongested conditions. When the average speed $\bar{v}(t)$ is greatly less than the free-flow speed v_{f}, the traffic is congested. Otherwise, the road is uncongested. When the road is congested, it is possible to estimate the backward shockwave speed $\hat{w}$ using equation (2.16). ℓ is the average car length, and τ is the average reaction time of drivers. The time when a shockwave can be observed is not common so it is difficult to get a good estimation of the average reaction time of drivers. If τ is not available, the headway between two consecutive vehicles is used. The measured value for capacity $\hat{Q}$ can be calculated based on the value of the shockwave speed, as shown in (2.17).

$$\hat{w} = \frac{\ell}{\tau} \tag{2.16}$$

$$\hat{Q} = \left(\frac{1}{v_{\mathrm{f}}} + \frac{1}{\hat{w}}\right) K \tag{2.17}$$

When the road is uncongested, the capacity is estimated first. Its value can be estimated with equation (2.18). In equation (2.18), $\min(\bar{h})$ represents the smallest headway in the section. The capacity is the largest number of vehicles that can pass a road section in an hour, which is equal to the number of smallest headways in an hour. A smaller headway corresponds to a larger flow rate and capacity. Then the backward shockwave speed $\hat{w}$ can be calculated based on the value of the capacity, as shown in (2.19). When the market penetration of equipped vehicles is low, the case in which one equipped vehicle follow another equipped vehicle should be found to extract the headway. If there is no such case in the current time step, the value of the capacity will not be updated.

$$\hat{Q} = \frac{3600}{\min(\bar{h})} \tag{2.18}$$

$$\hat{w} = \frac{K v_{\mathrm{f}}}{\hat{Q} v_{\mathrm{f}} - K} \tag{2.19}$$

2.3.3 The Structure of Kalman Filter

In this study, the update of parameters also uses a Kalman filter structure. $\mathbf{F}(t)$ is the vector of parameters at time t.

$$\mathbf{F}(t) = \begin{bmatrix} Q(t) \\ v_{\mathrm{f}}(t) \\ w(t) \end{bmatrix} \tag{2.20}$$

Equation (2.21) shows the updating process of these three parameters. $\mathbf{A_c}$ is an identity matrix because we assume that the prediction of parameters at time $t+1$ is just the values of parameters at time t, and the parameter value is a random walk.

$$\mathbf{F}(t+1) = \mathbf{A_c}\mathbf{F}(t) + \mathbf{Q_c}^* \tag{2.21}$$

The measurement vector $\hat{\mathbf{F}}$ is consisted of the measurements of the capacity, the free-flow speed and the backward shockwave speed. The method of getting the measurement is mentioned in section 2.3.2.

$$\hat{\mathbf{F}}(t) = \begin{bmatrix} \hat{Q}(t) \\ \hat{v}_{\mathrm{f}}(t) \\ \hat{w}(t) \end{bmatrix} \tag{2.22}$$

Kalman Gain is used to integrate these two parts, which is calculated by equation (2.23). In this equation, $\mathbf{C_r}$ is a 3×3 identity matrix, and the measurement of one parameter is assumed to be independent of those of other parameters.

$$\mathbf{K_c}(t+1) = \mathbf{P}_c(t+1|t)\mathbf{C_r}^\intercal \left[\mathbf{C_r}\mathbf{P}_c(t+1|t)\mathbf{C_r}^\intercal + \mathbf{R_c}\right]^{-1} \tag{2.23}$$

Using Kalman Gain $\mathbf{K_c}$, the values of predictions and measurements are integrated and the covariance matrix is updated with equations (2.24) and (2.25).

$$\mathbf{F}(t+1|t+1) = \mathbf{F}(t+1|t) + \mathbf{K_c}(t+1)\left[\hat{\mathbf{F}}(t+1) - \mathbf{C_c}\mathbf{F}(t+1|t)\right] \tag{2.24}$$

$$\mathbf{P_c}(t+1|t+1) = \mathbf{P_c}(t+1|t) - \mathbf{K_c}(t+1)\mathbf{C_c}\mathbf{P_c}(t+1|t) \tag{2.25}$$

2.4 Experiment

CTM simulators and microscopic simulators were used to generate multiple databases to test the proposed algorithm. In the test using CTM simulators, the research team tended to test the basic structure of the code, so a relatively high market penetration of 60% was used. In the test using the microscopic simulator, market penetrations of 20% and 40% were used.

2.4.1 Test with CTM simulator

Two test databases are generated by simulators based on CTM. The output of this simulator includes vehicle IDs, vehicle locations, and vehicle speeds at each time step. Vehicle locations

should be converted to the ID of the road segment that contains the vehicle. The output file only has the trajectories of a subset of the total vehicles. For example, if the market penetration is 60%, then the output file only includes the trajectories of 60% of the vehicles.

Test 1 with known parameters

Figure 2.2 shows a test with all parameters known. The orange line is the actual occupancy, and the blue line is the estimated occupancy. The penetration rate is 60%. The measured occupancy varies a lot and reaches zero at some time steps. It is because the input flow rate is 2 vehicles per time step and BSMs only provide data from 60% of the vehicles. Figure 2.2 reflects that if parameter values and the time of the incident are known, the CTM can be a good representation of the dynamics of the traffic flow generated by this simulator. For example, when there is a capacity drop at $t = 40$, the occupancy estimation is close to the actual occupancy of 8 vehicles, even though the measured occupancy of probe vehicles is 4. The prediction step based on CTM corrects the measurement of 4 vehicles (shown in Figure 2.3), and the final estimation for this road segment at time step 46 is calculated to be 7.6 (round to 8). The accuracy of the Kalman filter is higher when there is an incident compared with the free-flow condition. When there is an incident, the actual occupancy will be much higher than the measured occupancy of equipped vehicles and the Kalman filter will put more weight on the prediction step.

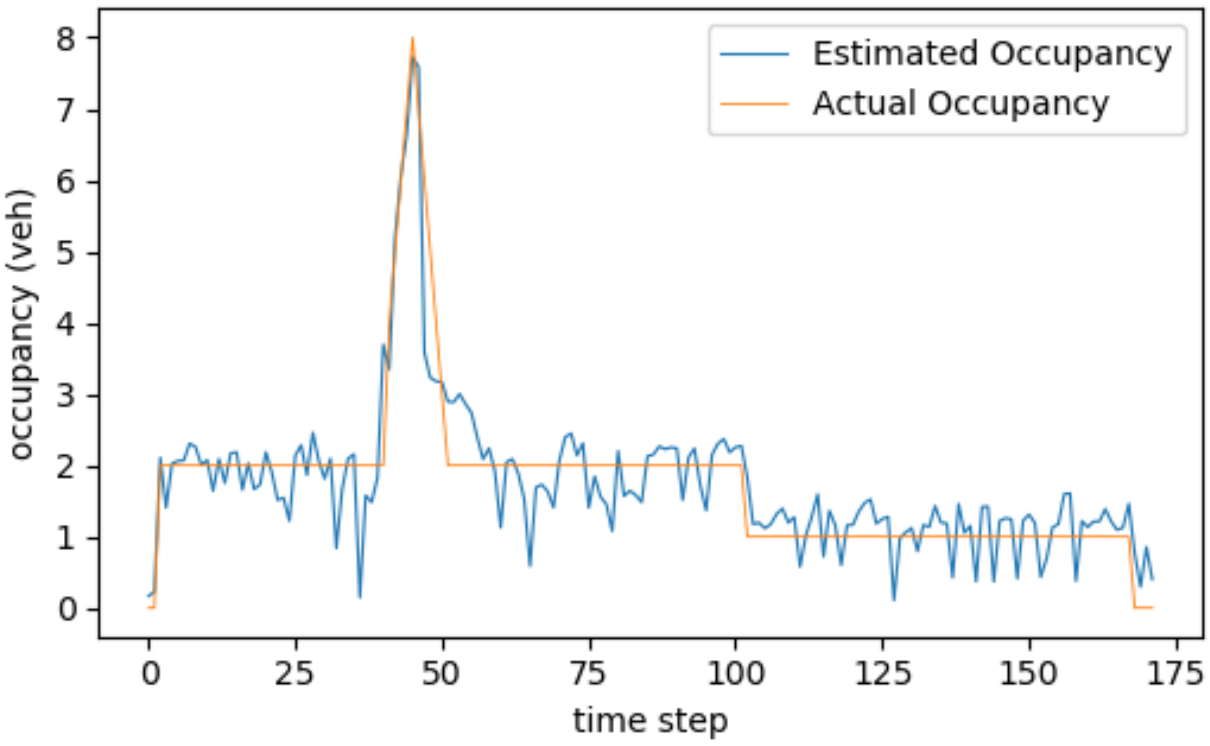

Figure 2.2: Test 1 with known parameters (estimated occupancy vs actual occupancy)

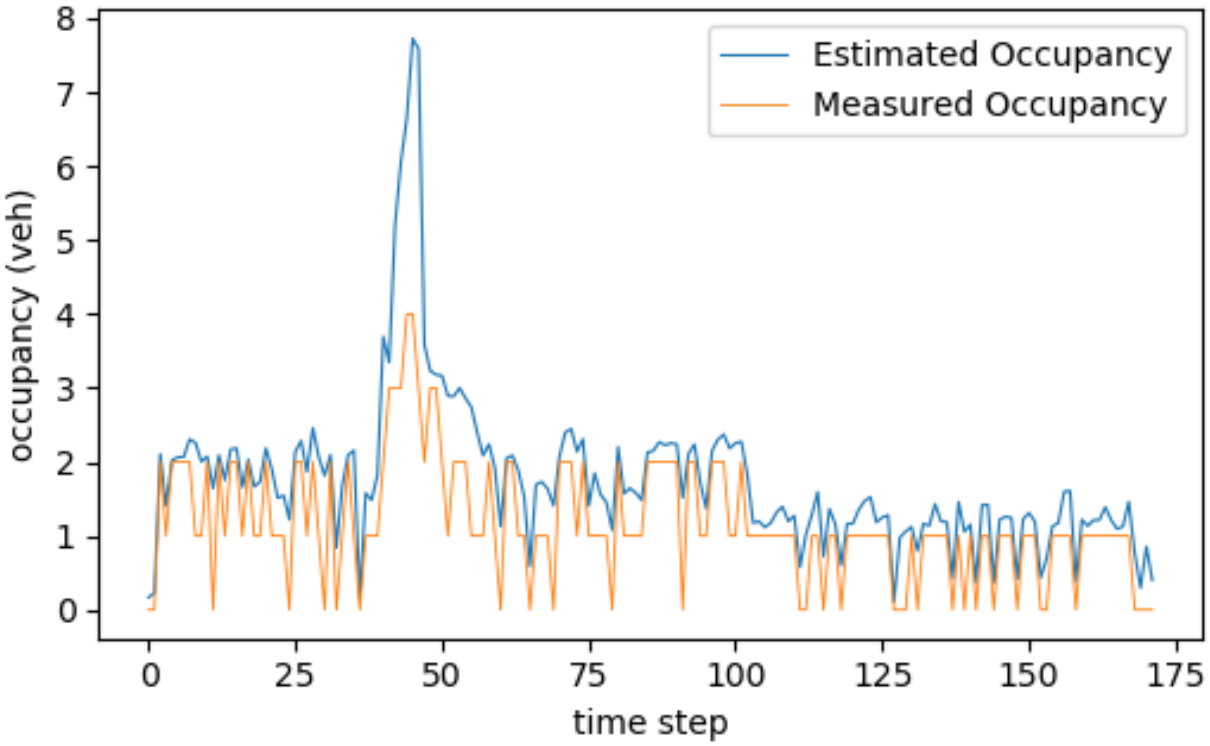

Figure 2.3: Test 1 with known parameters (estimated occupancy vs measured occupancy)

Figure 2.5 shows the estimated speed and measured speed of equipped vehicles. Figure 2.4 shows the estimated speed and the actual speed. The measured speed is slightly different from the actual speed. When there is no equipped vehicle at the current time step, the measured speed at last time step is used as the measured speed at the current time step, so it is possible that the actual speed has a big change but the measured speed remains the same. When there are few equipped vehicles in a road segment that behave differently from all the other vehicles in the same road segment, the measured speed and the actual speed will be different. In Figure 2.4, when the average speed is in free-flow speed, the Kalman filter sometimes overestimates the average speed. When there is a drop in the travel speed, the estimated speed is close to the actual speed. Compared with the occupancy, the speed estimation has higher occupancy. In practice, the travel speed is used to determine the level of service of the road. Traffic engineers are more focused on the speed estimation of the congestion condition than the free-flow condition. Therefore, the speed estimation in the Kalman filter can provide useful information in practice.

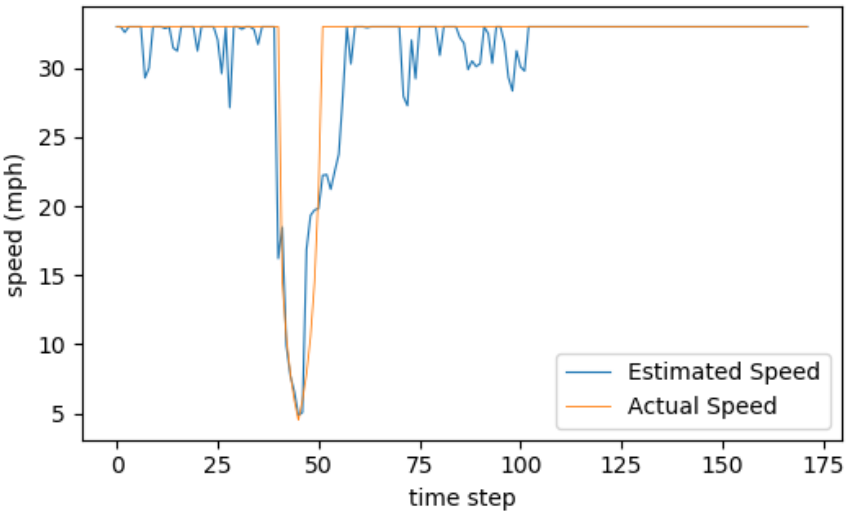

Figure 2.4: Test 1 with known parameters (estimated speed vs actual speed)

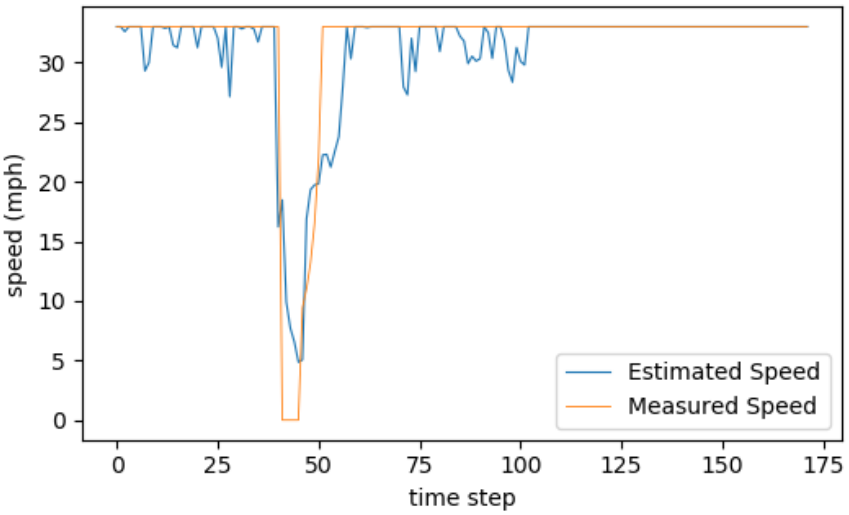

Figure 2.5: Test 1 with known parameters (estimated speed vs measured speed)

Test 2 with unknown parameters

In test 2, another CTM-based simulator was used to generate the test database. The values of parameters are unknown and the algorithm for parameter calibration runs simultaneously with the Kalman filter to get traffic state estimations. The market penetration rate is 65%. The results show that the free-flow speed is easier to calibrate than the capacity or congested wave speed. In Figure 2.8, the initial value of the free-flow speed is 30 miles per hour, but it converges to the actual value of free-flow speed in a short time. In this test, the capacity and the shockwave speed do not converge to their right values. The trajectory data generated

by the CTM-based simulator does not include enough information about the time gap or spacing between two vehicles. For capacity, it is not reasonable to use the maximum value of the flow rate for the value of capacity because the measured flow rate is only for equipped vehicles. For the backward shockwave speed, the calculation needs the reaction time between vehicles, which requires the case where two vehicles are close to each other. If there is no such case observed, the shockwave speed cannot be fully calibrated. In practice, the backward shockwave speed can also be calibrated by searching cases where two adjacent probe vehicles both have a drop in travel speed. With the time gap between two speed-drops and the distance between these two probe vehicles, the backward shockwave speed can be estimated.

If the parameters for CTM are not accurately calibrated, the prediction step of the Kalman filter will have limited accuracy. In Figure 2.6, the line representing estimation always follows the line representing the measurement. The estimation highly relies on the measurement step of the Kalman filter, which cannot represent the occupancy including all vehicles on the road. In Figure 2.7, from time step 75 to time step 183, the actual occupancy is always larger than the estimated occupancy.

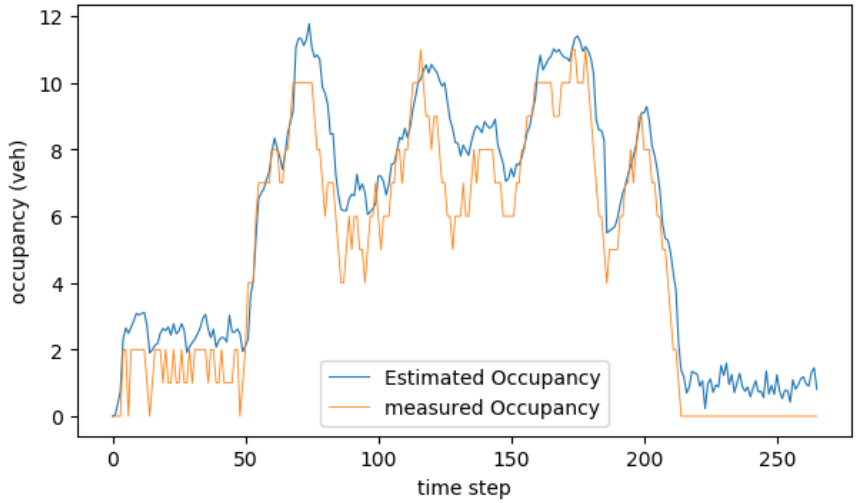

Figure 2.6: Test 2 with known parameters (estimated occupancy vs measured occupancy)

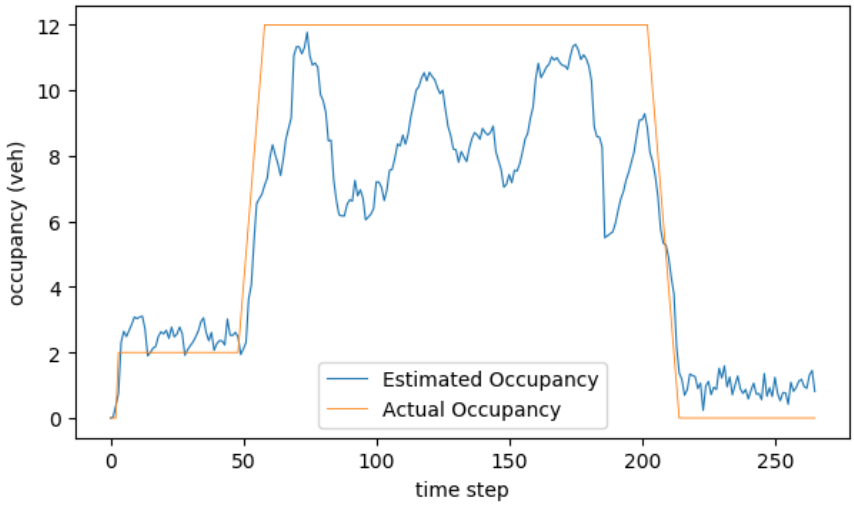

Figure 2.7: Test 2 with known parameters (estimated occupancy vs actual occupancy)

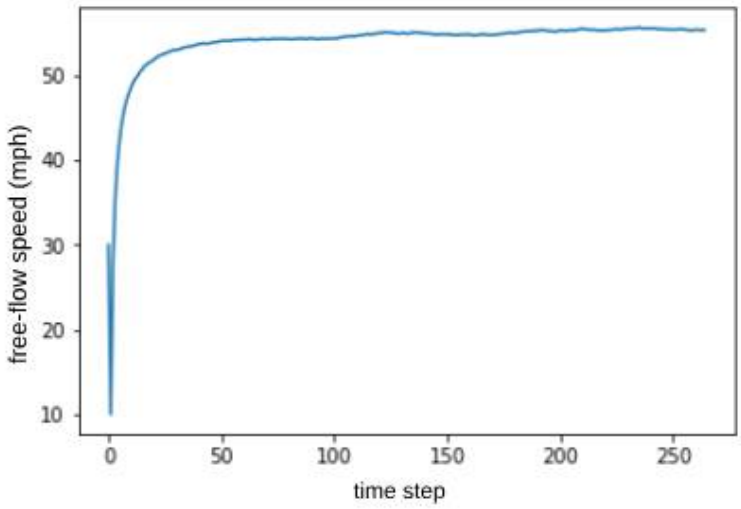

Figure 2.8: Calibration of free-flow speed in Test 2

2.4.2 Test with Microscopic Simulation Model (AIMSUN)

In this test, the microscopic simulation software AIMSUN was used to generate the database. Compared with the CTM simulator, the microscopic simulation model can generate drivers with more realistic driving behaviors and provide data that is more similar to actual BSM data. This database includes the speed, the coordination, and the heading direction of vehicles with a resolution of 0.1 seconds.

Figure 2.9 shows the microscopic simulation model in AIMSUN used for this test. This model covers all arterial roads and freeways in the city of Richfield, Minnesota and its

surrounding area. The target road section is shown in the red box in Figure 2.9. This road section is on the northbound of freeway I-35, with a length of 4158 feet.

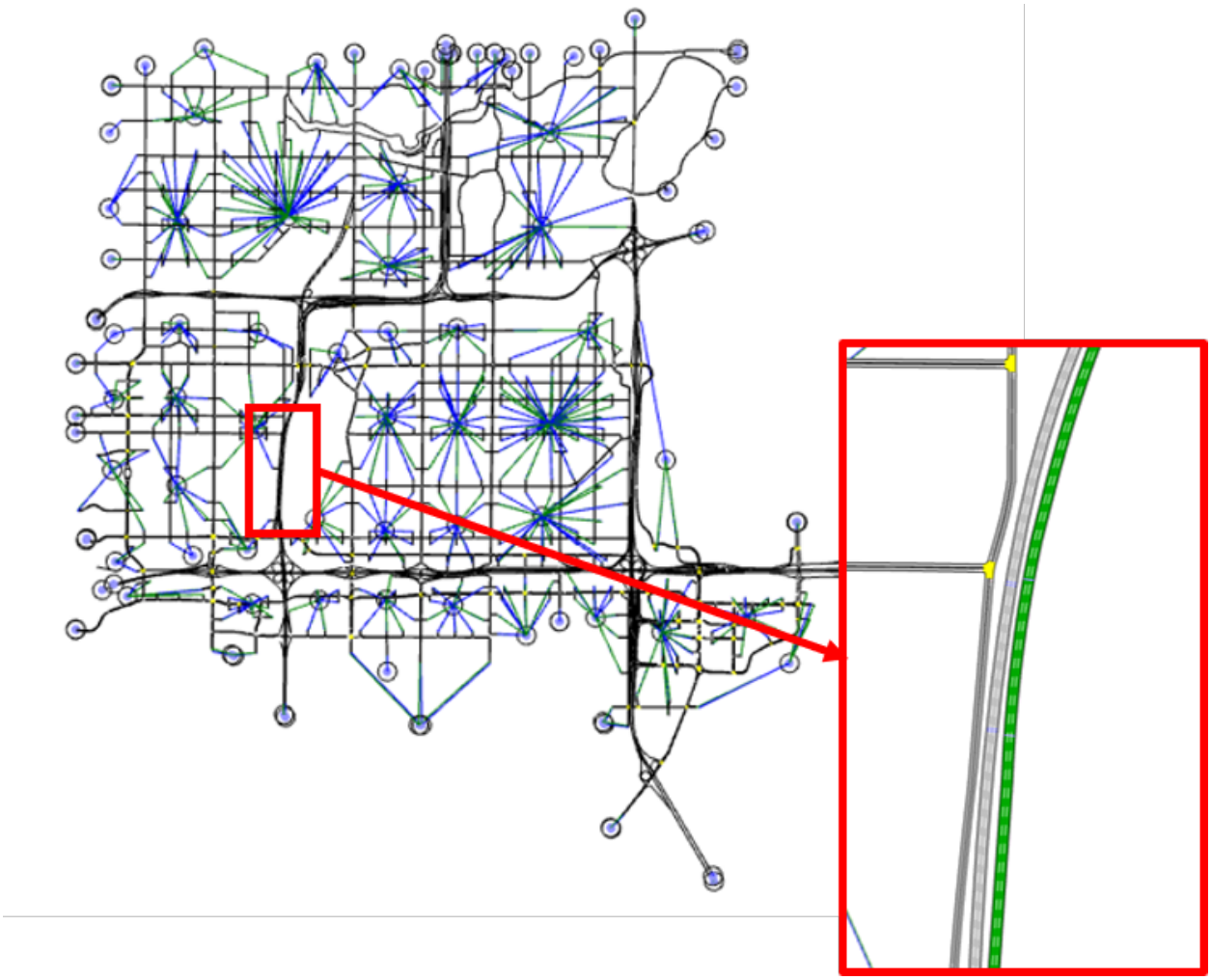

Figure 2.9: Example microsimulation model in AIMSUN

Data preprocessing work

To apply the database generated by the microscopic simulation model for the traffic state estimation, some data preprocessing works should be finished first.

If the location of the origin is known, the travel distance of a vehicle cannot be directly calculated using the current location (x,y) of this vehicle because the road section may be curved. It is more accurate to get the cumulative traveled distance along its trajectory, as shown in equation (2.26).

$$\text{Travel Distance} = \sum_{k=1}^{t-1} \sqrt{(x(k+1)-x(k))^2 + (y(k+1)-y(k))^2} \tag{2.26}$$

The trajectories of vehicles in the output of AIMSUN have a resolution of 0.1 second, but the required traffic state measurement is for a time interval that is equal to the time step of CTM. Therefore, Edie's definition of traffic state variables was applied to extract the traffic state from trajectory data, as shown in equations (2.27)–(2.30). x_i is the travel distance of vehicle i in a cell during a time interval. t_i is the travel time of vehicle i in a cell during a time interval. The area of a time-space zone $|A|$ is equal to the length of the road segment timing the duration of the time interval. Figure 2.10 shows the time-space zone used in Eddie's definition. To use equations (2.27)–(2.30) to extract the measurement of traffic state from vehicle trajectories, the trajectory of every vehicle should be extracted.

$$|A| = \Delta t \times \Delta L \tag{2.27}$$

$$q = \frac{\sum_i x_i}{|A|} \tag{2.28}$$

$$k = \frac{\sum_i t_i}{|A|} \tag{2.29}$$

$$v = \frac{\sum_i x_i}{\sum_i t_i} \tag{2.30}$$

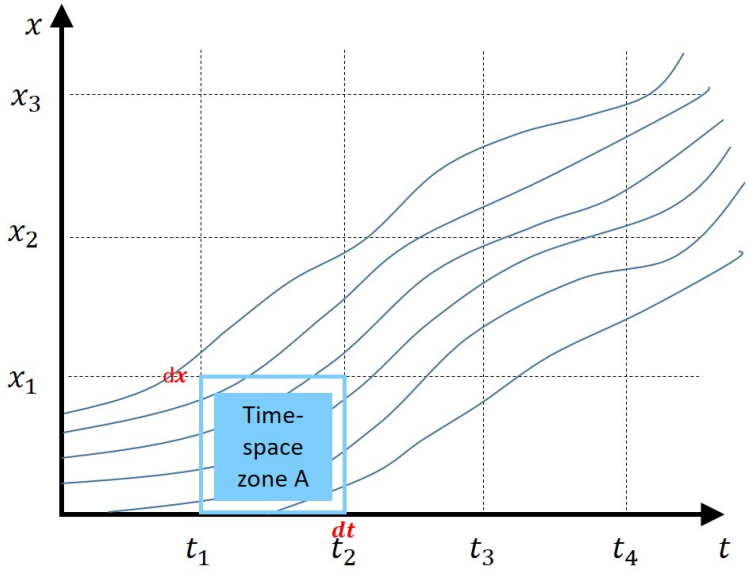

Figure 2.10: Time-space zone

Test 1 with calibrated parameters

In this test, the values of parameters are calibrated before the process of traffic state estimation. Two databases used in this test include vehicle trajectories for 20% and 40% of vehicles respectively. These two databases have vehicle trajectories generated by simulations

lasting 45 minutes. We have the third databased including the trajectories of all vehicles, not only probe vehicles. We considered the traffic state extracted from this database as the actual traffic state of the target road segment. By comparing the estimated traffic state with the actual traffics state, the error of the traffic estimation algorithm can be calculated by equation (2.31). In equation (2.31), N is the sample size, y_i is the actual value, and $\hat{y}_i$ is the estimated value.

$$e = \frac{1}{N} \sum_{1}^{N} \frac{|y_i - \hat{y}_i|}{y_i} \tag{2.31}$$

Figure 2.11 shows the estimated and actual occupancies for a road segment on the target road section. In this figure, the black dashed line representing the estimated occupancy roughly follows the trend of the orange solid representing the actual measured occupancy. The difference between these two lines gets larger when the occupancy of the road starts to increase. The calculated error is 35%. Figure 2.12 shows the estimated and actual speeds. Because the measurement of vehicle speed can be extracted from the vehicle trajectory, the accuracy of speed estimation is much higher than the occupancy, which is about 10%.

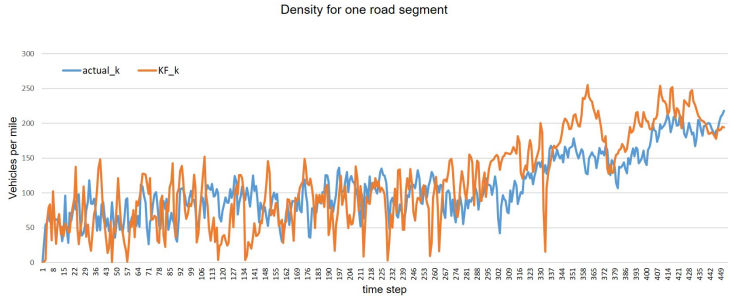

Figure 2.11: Test 1 with microscopic simulation model (estimated occupancy vs measured occupancy)

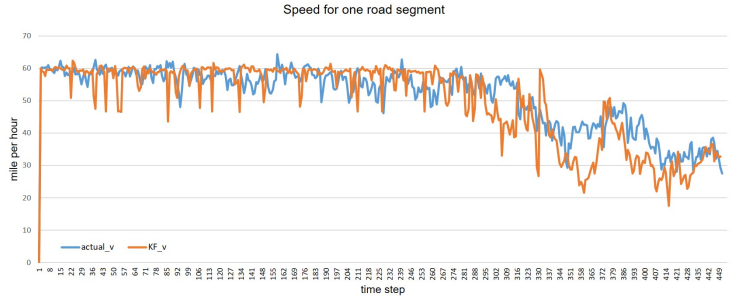

Figure 2.12: Test 1 with microscopic simulation model (estimated speed vs measured speed)

Figure 2.13 shows the estimated and actual occupancies when trajectories of 40% of vehicles are used. It is obvious that when the road segment becomes congested, the occupancy

estimation using 40% of vehicles is more accurate than the estimation using 20% of vehicles. The error e of occupancy estimation is 29%. Figure 2.14 shows the estimated and actual speeds. The error of speed estimation is 8%.

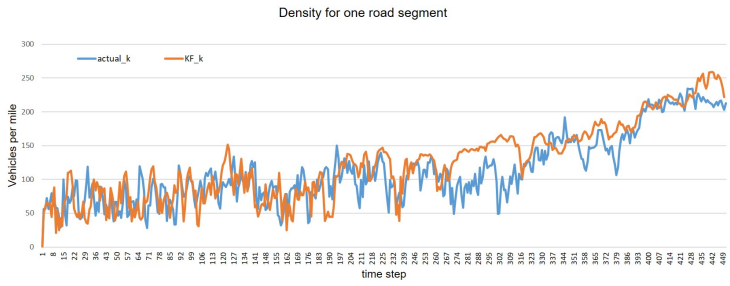

Figure 2.13: Test 1 with microscopic simulation model (estimated occupancy vs measured occupancy)

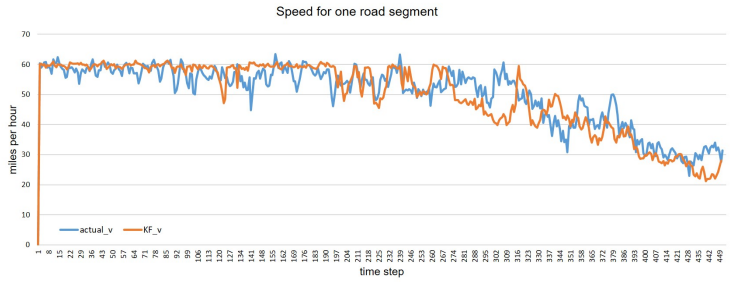

Figure 2.14: Test 1 with microscopic simulation model (estimated speed vs measured speed)

2.5 Future Work

In future work, the research team will use trajectory data from the microscopic simulation model and field data to test the accuracy of the Kalman filter. After that, the research team will decide whether loop detector data is needed to improve the estimation performance. The test data will include both congested and uncongested scenarios. Sensitivity analysis will also be conducted to discuss the effect of Kalman filter parameters on the model performance.

Chapter 3

Resilient Control under Cyber-Attacks and Sensor Health Monitoring in Connected ACC Vehicles

3.1 Introduction

Vehicle-to-vehicle (V2V) and infrastructure-to-vehicle (I2V) communication can provide a number of benefits to future intelligent vehicle system. These benefits include improvements in fuel economy using knowledge of future vehicle trajectories, enhancement of safety by blocking of shock wave propagation, and improvements in traffic capacity by enabling closer vehicle following (Rajamani and Zhu, 2002; Siegel et al., 2017; Lang et al., 2013). All of these benefits are obtained by enhancing currently available adaptive cruise control (ACC) systems using V2V and I2V communications!(Rajamani and Zhu, 2002; Siegel et al., 2017; Lang et al., 2013).

One of the most basic connected vehicle architectures involves the ACC vehicle communicating with just one other vehicle, its immediate preceding vehicle in the same lane. Results published about 15 years ago show how string stability can be enhanced by this inter-vehicle communication (Rajamani and Zhu, 2002). Such a system was called a "semi-autonomous adaptive cruise control (SA-ACC)" system in Rajamani and Zhu (2002). Specifically, the allowable time-gap between vehicle h is normally required to be no smaller than the value

$$h > 2\tau \tag{3.1}$$

where τ is the time constant of the vehicle's lower loop dynamics involving the engine and driveline system (Rajamani, 2011a). However, if inter-vehicle communication from the immediately preceding vehicle is available (i.e., the preceding vehicles acceleration is wirelessly transmitted to the ACC vehicle), then the time gap can be made much smaller and higher traffic flow can be achieved with no risk of shock wave propagation. This is because (3.1) no

longer has to be satisfied.

This chapter relates to SA-ACC systems and develops an estimation algorithm that can detect cyber-attacks on the communication channel from the preceding vehicle and can also monitor the health of the radar sensor. An elegant solution that decouples the cyber-attack signal in the failures from the estimation error dynamics is developed. It should be noted that potential attack threats on inter-vehicular communication systems and on sensor systems have been discussed previously in literature (Petit and Shladover, 2014; van der Heijden et al., 2017; Parkinson et al., 2017). False data injection and denial of service attack can lead to significant problems in autonomous vehicles and connected vehicle systems that use inter-vehicular communication. Also, sensor faults can be a serious source of problems for many intelligent transportation systems. An attacker can obtain access to the internal system of the vehicle or transmit false data to the control system. Thus, it is necessary to have a resilient system for autonomous and/or connected vehicles that can be secure against cyber-attacks and sensor faults. Recently, several researchers have focused on cyber-attacks and sensor fault problems for connected vehicle systems. For an autonomous vehicle using an acceleration sensor and a radar, a sliding mode observer is used to detect sensor faults in Oh et al. (2018). In Boukhari et al. (2018), two different observer techniques are proposed to estimate a vehicles speed sensor fault. Authors in Biron et al. (2018) proposed a sliding mode observer to detect and estimate denial of service attack for a connected vehicle. False data injection on acceleration information via V2V communication and sensor (LIDAR or radar) faults are considered and Hidden Markov Model-based attack detection method is proposed for cooperative adaptive cruise control applications in Jagielski et al. (2018). Most papers in literatures handle either cyber-attacks or sensor faults.

The remainder of this chapter is organized as follows. In Section 3.2, a brief review of the SA-ACC system is provided. In Section 3.3, a model based on measurable states is developed from the SA-ACC system. An observer for cyber-attack and sensor fault estimation is proposed in Section 3.4. Results of simulation studies and discussion is presented in Section 3.5. Conclusions are presented in Section 3.6.

3.2 SA-ACC System

The SA-ACC system aims to obtain high traffic capacity and small inter-vehicle spacing while using communication from only the preceding vehicle on the highway. The constant time gap spacing policy is utilized to design the controller of the SA-ACC system. In the presence of actuator dynamics represented by a first-order lag, the vehicle model of the SA-ACC vehicle is described as

$$\tau \dddot{x}_i + \ddot{x}_i = u_{syn} \tag{3.2}$$

where τ is a lag constant associated with the lower dynamics of the vehicle, x_i is the ith vehicle position and u_{syn} is the control input of the ith vehicle. If the SA-ACC vehicle maintained a constant distance from the preceding vehicle, then the spacing error for the ith

vehicle in a string of vehicles would be defined as

$$\epsilon_i = x_i - x_{i-1} + L_i \tag{3.3}$$

where L_i would be the desired constant spacing between vehicles. However, a controller designed by using the constant spacing policy based on (3.3) would need wireless access to the lead vehicle speed and acceleration, in addition to preceding vehicle acceleration in order to maintain string stability in a string of autonomous vehicles. Therefore, in order to avoid requiring communication from the lead vehicle, the constant time-gap spacing policy is utilized to design a controller using only preceding vehicle information. The desired spacing between vehicles in the constant time-gap spacing policy is not constant but is linear function of speed:

$$\text{Desired spacing} = L_i + h\dot{x}_i \tag{3.4}$$

where L_i is a constant and h is time gap. The spacing error in the constant time-gap spacing policy is therefore

$$\bar{\epsilon}_i = \epsilon_i + h\dot{x}_i = x_i - x_{i-1} + L_i + h\dot{x}_i \tag{3.5}$$

Based on (3.5), the controller is given by

$$u_{syn} = -k_1\ddot{x}_{i-1} + (k_1 + hk_1k_2)\ddot{x}_i - \frac{1}{h}(1 - hk_1k_2)\dot{\epsilon}_i - \frac{k_2}{h}\epsilon_i - k_2\dot{x}_i \tag{3.6}$$

where $\ddot{x}_{i-1}$ is the acceleration of the preceding vehicle obtained by using inter-vehicle communication. k_1 and k_2 are controller design parameters. A detailed procedure to obtain the controller and determine its parameters can be found in Rajamani and Zhu (2002).

3.3 New Model for SA-ACC System

In this section, we develop a model incorporating relative motion between the preceding and following vehicle with the following vehicle using the SA-ACC system. The model is in terms of measurable variables (relative distance and velocity between the vehicles). Also, model for false data injection and denial of service cyber-attacks is presented.

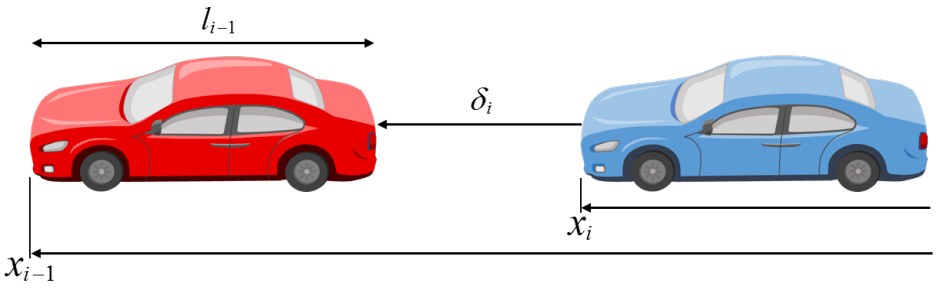

Figure 3.1: Preceding and following vehicles

3.3.1 SA-ACC System Model

As shown in Figure 3.1, the radar-measured spacing distance for the ith vehicle to the preceding vehicle can be defined as

$$\delta_i = x_{i-1} - x_i - l_{i-1} \tag{3.7}$$

where l_{i-1} is the length of the preceding vehicle. Then, we have

$$\begin{aligned} \dot{\delta}_i &= \dot{x}_{i-1} - \dot{x}_i \\ \ddot{\delta}_i &= \ddot{x}_{i-1} - \ddot{x}_i \\ \dddot{\delta}_i &= \dddot{x}_{i-1} - \dddot{x}_i \end{aligned} \tag{3.8}$$

By using (3.7) and (3.8), the controller becomes

$$u_{syn} = (hk_1k_2)\ddot{x}_{i-1} - k_2\dot{x}_i - (k_1 + hk_1k_2)\ddot{\delta}_i + \frac{1}{h}(1 - hk_1k_2)\dot{\delta}_i + \frac{k_2}{h}\delta_i - \frac{k_2}{h}(L_i - l_{i-1}) \tag{3.9}$$

Fortunately, the time lag constant associated with the preceding vehicle does not need to be known, since we directly obtain the acceleration information of the preceding vehicle using wireless communication. Thus, without considering its lower order dynamics, the preceding vehicle model can be represented as

$$\begin{aligned} \ddot{x}_{i-1} &= a_{i-1} \\ \dddot{x}_{i-1} &= 0 \end{aligned} \tag{3.10}$$

Substituting from (3.9) into (3.2) and using (3.10), we obtain

$$\begin{aligned} \dddot{\delta}_i = \frac{1}{\tau}(1 - hk_1k_2)a_{i-1} - \frac{1}{\tau}(1 - k_1 - hk_1k_2)\ddot{\delta}_i \\ - \frac{1}{\tau h}(1 - hk_1k_2)\dot{\delta}_i - \frac{k_2}{\tau h}\delta_i + \frac{k_2}{\tau}\dot{x}_i + \frac{k_2}{\tau h}(L_i - l_{i-1}) \end{aligned} \tag{3.11}$$

Finally, with a state vector $x = \begin{bmatrix} \delta_i & \dot{\delta}_i & \ddot{\delta}_i \end{bmatrix}^T$, we have state space model:

$$\begin{aligned} \begin{bmatrix} \dot{\delta}_i \\ \ddot{\delta}_i \\ \dddot{\delta}_i \end{bmatrix} = \begin{bmatrix} 0 & 1 & 0 \\ 0 & 0 & 1 \\ -\frac{k_2}{\tau h} & -\frac{k_3}{\tau h} & \frac{(k_1-k_3)}{\tau h} \end{bmatrix} \begin{bmatrix} \delta_i \\ \dot{\delta}_i \\ \ddot{\delta}_i \end{bmatrix} \\ + \begin{bmatrix} 0 \\ 0 \\ \frac{k_2}{\tau} \end{bmatrix} \dot{x}_i + \begin{bmatrix} 0 \\ 0 \\ \frac{k_3}{\tau} \end{bmatrix} a_{i-1} + \begin{bmatrix} 0 \\ 0 \\ \frac{k_2(L_i - l_{i-1})}{h} \end{bmatrix} \frac{1}{\tau} \end{aligned} \tag{3.12}$$

where k_3 is $1 - hk_1k_2$. $\dot{x}_i$ can be easily obtained by using sensors on the vehicle anda_{i-1} is obtained by using inter-vehicle communication that can be the subject of cyber-attack.

Since a radar measures the relative distance and velocity, we have output equation as

$$y = \begin{bmatrix} 1 & 0 & 0 \\ 0 & 1 & 0 \end{bmatrix} \begin{bmatrix} \delta_i \\ \dot{\delta}_i \\ \ddot{\delta}_i \end{bmatrix} \tag{3.13}$$

Equation (3.12) and (3.13) can be represented by the following compact form:

$$\begin{aligned} \dot{x} &= Ax + Bu + Fa_{i-1} + \Delta \\ y &= Cx \end{aligned} \tag{3.14}$$

where

$$\begin{aligned} A &= \begin{bmatrix} 0 & 1 & 0 \\ 0 & 0 & 1 \\ -\frac{k_2}{\tau h} & -\frac{k_3}{\tau h} & \frac{(k_1-k_3)}{\tau} \end{bmatrix} \\ B &= \begin{bmatrix} 0 \\ 0 \\ \frac{k_2}{\tau} \end{bmatrix} \\ F &= \begin{bmatrix} 0 \\ 0 \\ \frac{k_3}{\tau} \end{bmatrix} \\ \Delta &= \begin{bmatrix} 0 \\ 0 \\ \frac{k_2(L_i-l_{i-1})}{\tau h} \end{bmatrix} \\ C &= \begin{bmatrix} 1 & 0 & 0 \\ 0 & 1 & 0 \end{bmatrix} \end{aligned} \tag{3.15}$$

Now, we also consider the model for two classes of cyber-attacks (false data injection and denial of service attacks) on the inter-vehicle wireless communication.

3.3.2 Cyber-Attack Model

We introduce a new variable μ as the signal (transmitted data: acceleration of preceding vehicle) obtained from inter-vehicle communication. Thus, the system model becomes

$$\begin{aligned} \dot{x} &= Ax + Bu + F\mu + \Delta \\ y &= Cx \end{aligned} \tag{3.16}$$

False data injection attacks transmit false data to the control system or modify the transmitted data in the control system. Since the transmitted data can be corrupted by the

false data injection attack, μ is defined as

$$\mu = a_{i-1} + f_a \tag{3.17}$$

Denial of Service (DoS) attacks can keep the inter-vehicle communication network busy and can cause delays and congestions in the inter-vehicle communication channel. Therefore, the denial of service attacks can be modeled as the delay signal:

$$\mu(t) = a_{i-1}(t - \tau_d) \tag{3.18}$$

where τ_d is unknown delay. By applying Taylor's theorem to (3.18) and assuming higher order terms negligible, the delay signal can be approximated as

$$\mu(t) \approx a_{i-1}(t) - \tau_a \dot{a}_{i-1}(t) \tag{3.19}$$

Using the notation $f_d = -\tau_d \dot{a}_{i-1}(t)$ and omit time variable t for the sake of simplicity, the delay signal can be presented as

$$\mu = a_{i-1} + f_d \tag{3.20}$$

It is noted that (3.20) has the same structure as (3.17). Therefore, the two classes of the cyber-attacks can be modeled as

$$\mu = a_{i-1} + f_c \tag{3.21}$$

where f_c is either f_a or f_d. It is noted that f_c is assumed to be a constant or slowly varying.

3.4 Observer and Controller for Resilient SA-ACC System

Instead of using the system model (3.16), we develop a model for the detection of cyber-attacks and sensor faults. The model involves cyber-attack and sensor fault terms. As a result, an observer designed corresponding the model can be developed to estimate the unknown cyber-attack and sensor fault terms so as to detect the cyber-attacks and sensor faults. The model is derived based on two assumptions.

First, we assume that the system is not corrupted by cyber-attacks (the system rejects cyber-attacks).

Second assumption is that sensor fault occurs only at the velocity measurement channel of the radar.

Based on the assumptions and using (3.21), the model (3.16) can be presented with unknown inputs f_c and f_s

$$\begin{aligned} \dot{x} &= Ax + Bu + F\mu + \Delta - Ff_c \\ y &= Cx + Df_s \end{aligned} \tag{3.22}$$

where $D = \begin{bmatrix} 0 & 1 \end{bmatrix}^T$. By estimating unknown inputs f_c and f_s, the cyber-attack and sensor

fault can be detected.

An unknown input observer that can estimate states and unknown inputs will be presented and we will discuss how to detect the cyber-attack and sensor fault in both range and velocity measurement channels. Then, resilient control method under the cyber-attack will be proposed.

For unknown input estimation, a number of observer design methods have been proposed in literature. A proportional-integral observer was proposed to estimate the states and unknown inputs in Bakhshande and Söffker (2015). An unknown input estimation method based on nonlinear observer design and dynamic model inversion is proposed in Phanomchoeng and Rajamani (2013). Another approach is designing observer for descriptor system that adding unknown input to the state vector Phanomchoeng et al. (2018). In this chapter, an observer design method based on descriptor systems is proposed to detect and estimate the unknown inputs due to cyber-attacks and sensor faults.

3.4.1 Descriptor System for Radar Sensor Fault

In order to deal with the radar sensor fault, f_s is considered as a state of the system. Using the new state vector, original system is converted to the descriptor system form. The state vector with f_s is defined as

$$\xi = \begin{bmatrix} \delta_i & \dot{\delta}_i & \ddot{\delta}_i & f_s \end{bmatrix}^T \tag{3.23}$$

With the state vector (3.23), the system (3.22) is rewritten under the descriptor from:

$$\begin{aligned} E\dot{\xi} &= A_e\xi + Bu + F\mu + \Delta - Ff_c \\ y &= C_e\xi \end{aligned} \tag{3.24}$$

Detailed matrices in (3.24) are defined as

$$\begin{aligned} E &= \begin{bmatrix} I_{n_x} & 0 \end{bmatrix} \\ A_e &= \begin{bmatrix} A & 0 \end{bmatrix} \\ C_e &= \begin{bmatrix} C & D \end{bmatrix} \end{aligned} \tag{3.25}$$

where I_{n_x} is the identity matrix of dimension n_x (size of state vector x).

Since the matrix D is full column rank, the following condition holds:

$$rank\left(\begin{bmatrix} E \\ C_e \end{bmatrix}\right) = rank\left(\begin{bmatrix} I_{n_x} & 0 \\ C & D \end{bmatrix}\right) = n_\xi \tag{3.26}$$

3.4.2 Unknown Input Observer for Cyber-Attack and Sensor Fault Estimation

Let us consider the following observer structure to estimate states and unknown inputs simultaneously:

$$\begin{aligned}\dot{z} &= Nz + Ly + Mu + G\mu + T\hat{f}_c + P_z\Delta \\ \hat{\xi} &= z + Q_z y \\ \dot{\hat{f}}_c &= H\left(y - \hat{y}\right)\end{aligned} \tag{3.27}$$

The matrices N, L, M, G, T, P_z, Q_z and H are observer parameters to be designed such that the estimation error $\tilde{\xi} = \xi - \hat{\xi}$ converges towards zero.

By using (3.24) and (3.27), the estimation error is

$$\tilde{\xi} = (I - Q_z C_e)\xi - z \tag{3.28}$$

From the rank condition (3.26), there exist matrices P_z and Q_z such that

$$P_z E + Q_z C_e = I_{n_x} \tag{3.29}$$

Also, P_z and Q_z can be computed as follows:

$$\left[\begin{array}{cc} P_z & Q_z \end{array}\right] = \left(\left[\begin{array}{c} E \\ C_e \end{array}\right]^T \left[\begin{array}{c} E \\ C_e \end{array}\right]\right)^{-1} \left[\begin{array}{c} E \\ C_e \end{array}\right]^T \tag{3.30}$$

Therefore, the estimation error dynamics can be written as

$$\dot{\tilde{\xi}} = P_z E\dot{\xi} - \dot{z} \tag{3.31}$$

Theorem 1. *Consider the system* (3.24) *and observer* (3.27). *If there exist the symmetric matrix* $P > 0$ *and the matrix* R *of appropriate dimensions such that*

$$\begin{aligned} N &= P_z A_e - K C_e \\ L &= K + N Q_z \\ M &= P_z B \\ G &= P_z F \\ T &= -P_z F \end{aligned} \tag{3.32}$$

and

$$\left[\begin{array}{cc} P_z A_e & -P_z F \\ 0 & 0 \end{array}\right]^T P + P \left[\begin{array}{cc} P_z A_e & -P_z F \\ 0 & 0 \end{array}\right] - \left[\begin{array}{cc} C_e & 0 \end{array}\right]^T R - R^T \left[\begin{array}{c} C_e 0 \end{array}\right] + 2\alpha P \leq 0 \tag{3.33}$$

then, the observer gain $\begin{bmatrix} K & H \end{bmatrix}^T$ *is given by*

$$\begin{bmatrix} K & H \end{bmatrix}^T = P^{-1}R^T \tag{3.34}$$

and with this value of the observer gain, the estimation error of the observer (3.27) *converges exponentially towards zero. Therefore, the observer can estimate both unknown inputs due to the cyber-attacks and sensor faults simultaneously.*

Proof. Using the system (3.24) and observer (3.27), the estimation error dynamics (3.31) is rewritten as

$$\dot{\tilde{\xi}} = N\tilde{\xi} + (P_z A_e - N - LC_e + NQ_z C_e)\xi + (P_z B - M)u + (P_z F - G)\mu - P_z F f_c - T\hat{f}_c \tag{3.35}$$

The observer parameters are defined as (3.32). Then, (3.35) becomes

$$\dot{\tilde{\xi}} = (P_z A_e - KC_e)\tilde{\xi} - P_z F\tilde{f}_c \tag{3.36}$$

Using (3.27) and the assumption that $f_c = 0$, we have augmented system:

$$\begin{bmatrix} \dot{\tilde{\xi}} \\ \dot{\tilde{f}}_c \end{bmatrix} = \begin{bmatrix} (P_z A_e - KC_e) & -P_z F \\ -HC_e & 0 \end{bmatrix} \begin{bmatrix} \tilde{\xi} \\ \tilde{f}_c \end{bmatrix} \tag{3.37}$$

Rearrange (3.37), then we have

$$\begin{bmatrix} \dot{\tilde{\xi}} \\ \dot{\tilde{f}}_c \end{bmatrix} = \left[\begin{bmatrix} P_z A_e & -P_z F \\ 0 & 0 \end{bmatrix} - \begin{bmatrix} K \\ H \end{bmatrix} \begin{bmatrix} C_e & 0 \end{bmatrix} \right] \begin{bmatrix} \tilde{\xi} \\ \tilde{f}_c \end{bmatrix} \tag{3.38}$$

It should be noted that the estimation error dynamics is decoupled from u and μ. Thus, the observer (3.27) is allowed to estimate the state of the system and unknown inputs independently of the signal that may be corrupted by cyber-attacks or sensor faults.

In order to find a gain for the exponential stable system for (3.38), we require that the following differential inequality is satisfied:

$$\dot{V} \leq -2\alpha V \tag{3.39}$$

where V is the Lyapunov function candidate defined as

$$V = \begin{bmatrix} \tilde{\xi} \\ \tilde{f}_c \end{bmatrix}^T P \begin{bmatrix} \tilde{\xi} \\ \tilde{f}_c \end{bmatrix} \tag{3.40}$$

for observer design and α is a positive constant. The inequality (3.39) implies the exponential stability of the system Khalil and Grizzle (2002). By calculating the derivative of the

Lyapunov function, we have

$$\dot{e}^T P e + e^T P \dot{e} + 2\alpha e^T P_e \leq 0 \tag{3.41}$$

where $e = \begin{bmatrix} \tilde{\xi} \\ \tilde{f} \end{bmatrix}^T$. (3.41) is satisfied when following condition is satisfied:

$$\left[\begin{bmatrix} P_z A_e & -P_z F \\ 0 & 0 \end{bmatrix} - \begin{bmatrix} K \\ H \end{bmatrix} \begin{bmatrix} C_e & 0 \end{bmatrix}\right]^T P + P\left[\begin{bmatrix} P_z A_e & -P_z F \\ 0 & 0 \end{bmatrix} - \begin{bmatrix} K \\ H \end{bmatrix} \begin{bmatrix} C_e & 0 \end{bmatrix}\right] + 2\alpha P \leq 0 \tag{3.42}$$

By introducing a new variable $R = \begin{bmatrix} K & H \end{bmatrix} P$, (3.42) becomes

$$\begin{bmatrix} P_z A_e & -P_z F \\ 0 & 0 \end{bmatrix}^T P + P \begin{bmatrix} P_z A_e & -P_z F \\ 0 & 0 \end{bmatrix} - \begin{bmatrix} C_e & 0 \end{bmatrix}^T R - R^T \begin{bmatrix} C_e & 0 \end{bmatrix} + 2\alpha P \leq 0 \tag{3.43}$$

□

3.4.3 Cyber-Attack and Sensor Fault Detection

In this section, we discuss how to detect cyber-attacks and sensor faults based on the estimated terms $\hat{f}_c$ and $\hat{f}_s$ from the proposed unknown input observer.

If there are no cyber-attack and sensor fault i.e., (3.22) is the same as actual system (3.14), estimated unknown inputs $\hat{f}_c$ and $\hat{f}_s$ converge to zero. If cyber-attack exists ($f_c \neq 0$), $\hat{f}_c$ becomes non-zero and cyber-attack can be detected. It is noted that $\hat{f}_c$ may not converge to true value due to discrepancy between the actual system and the system model for the observer. However, still $\hat{f}_c$ can be used to detect the cyber-attack since $\hat{f}_c$ cannot be zero under the cyber-attack.

If sensor fault occurs, non-zero value of $\hat{f}_s$ is obtained from the observer. Although the observer estimates only the sensor fault term in the velocity measurement channel of the radar, the sensor fault in the range measurement channel can be detected. Since the model (3.22) is based on the assumption that the sensor fault occurs only in the velocity measurement channel, the observer relies more on the range measurement (larger gain for the range measurement) and estimates states and unknown inputs. In other words, if a sensor fault occurs at the range measurement channel, the observer provides non-zero value of $\hat{f}_s$ since the estimates are computed from wrong range measurements. It is noted that $\hat{f}_c$ may not be zero due to discrepancy between the actual system and the system model for the observer even though cyber-attack does not occur.

As a result, we propose two-step approach to detect cyber-attacks or sensor faults. First, the system checks the value of $\hat{f}_s$ to find if there exist any sensor faults. If the value of $\hat{f}_s$ exceeds certain threshold, i.e., sensor fault occurs at either or both range and velocity channels of the radar, the system alerts the driver and changes to manual driving from SA-

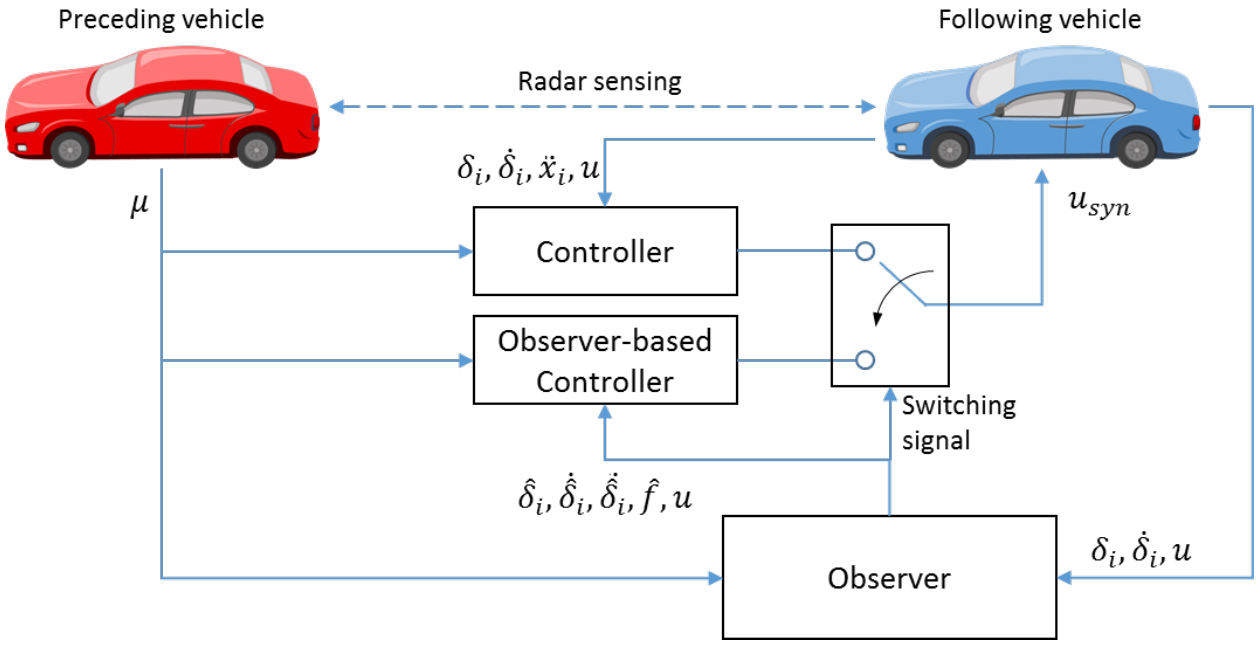

Figure 3.2: Resilient control for SA-ACC system.

ACC operation. Second, if there is no sensor fault, the system checks the value of $\hat{f}_c$. If the value of $\hat{f}_c$ exceeds certain threshold, i.e., cyber-attack occurs, the system switches a controller and can achieve resilient control for SA-ACC system, as shown in Figure 3.2.

3.4.4 Controller for Resilient SA-ACC System

Resilient control for SA-ACC system can be accomplished by utilizing the controller follow, instead of using the controller (3.6):

$$u_{syn} = (hk_1k_2)\mu - k_2\dot{x}_i - (k_1 + hk_1k_2)\ddot{\hat{\delta}}_i + \frac{1}{h}(1 - hk_1k_2)\dot{\hat{\delta}}_i + \frac{k_2}{h}\hat{\delta}_i - \frac{k_2}{h}(L_i - l_{i-1}) - (hk_1k_2)\hat{f}_c \quad (3.44)$$

This controller leads the actual system to exact match with the model (3.22). Hence, the proposed unknown input observer with the controller (3.44) guarantees that the estimation error of states and unknown inputs converges exponentially towards zero, and accomplishes resilient control for SA-ACC under the cyber-attack. Since the controller uses estimates, string stability may not be guaranteed. Therefore, we utilize larger value of h which satisfies (3.1) to maintain string stability.

3.5 Simulation Studies and Discussion

The developed observer based on the descriptor system for the cyber-attack and sensor fault detection and controllers described in the previous section has been evaluated using simulations. For the SA-ACC system the system and controller parameters are $\tau = 0.4$, $l_{i-1} = 5$, $L_i = 7.3$, $h = 0.5$, $k_1 = -0.8$, $k_2 = 2.5$ and $k_3 = 2$.

We solve (3.32) – (3.34) for the observer gain using the LMI toolbox in MATLAB. The observer gain is with the exponential stability parameter $\alpha = 3.5$:

$$K = \begin{bmatrix} 17.3524 & 4.5678 \\ 237.1617 & 64.2509 \\ 271.4056 & 69.4228 \\ -244.0019 & -60.2509 \end{bmatrix}$$
$$H = \begin{bmatrix} -762.0394 & -196.6185 \end{bmatrix} \tag{3.45}$$

The preceding vehicle is initially driving with 10m/s and the following vehicle is stopped and the initial distance between the preceding and following vehicles is 10m. Gaussian noise $\mathcal{N}(06^2[cm])$ and $\mathcal{N}(0, 60^2[cm/s])$ are added to the range and velocity measurements respectively. The upper and lower values of the thresholds for sensor fault and cyber-attack detection are set as ± 3. In practice, the threshold can be set based on the sensor noise. If the system switches the controller to (3.49) for resilient control under cyber-attacks, we utilize 1 for the value of h, which satisfies $h > 2\tau$.

3.5.1 Simulation Results with Sensor Faults

We evaluate the performance of the proposed observer for the radar sensor fault detection. The sensor fault is modeled by adding false data f_r and f_v to the range measurement and the velocity measurement respectively. First, we consider the sensor fault in the velocity measurement channel of the radar. The sensor fault is generated as

$$f_v = \begin{cases} 10 & t \geq 0 \\ 0 & \text{otherwise} \end{cases} \tag{3.46}$$

Due to the sensor fault, the following vehicle perceives an abrupt increase of the velocity of the preceding vehicle. As shown in Figure 3.3, the following vehicle is controlled to increase the velocity of the vehicle to maintain the desired distance based on the wrong information. As a result, collision ($\delta_i \leq 0$) occurs at 19.28 seconds as shown in Fig. 3.3. Fig. 3.4 shows the results of the proposed observer. The proposed observer successfully estimates the false data due to the sensor fault in the velocity channel of the radar and detect the fault immediately at 10 seconds.

Second, we consider the sensor fault in the range measurement channel of the radar. The

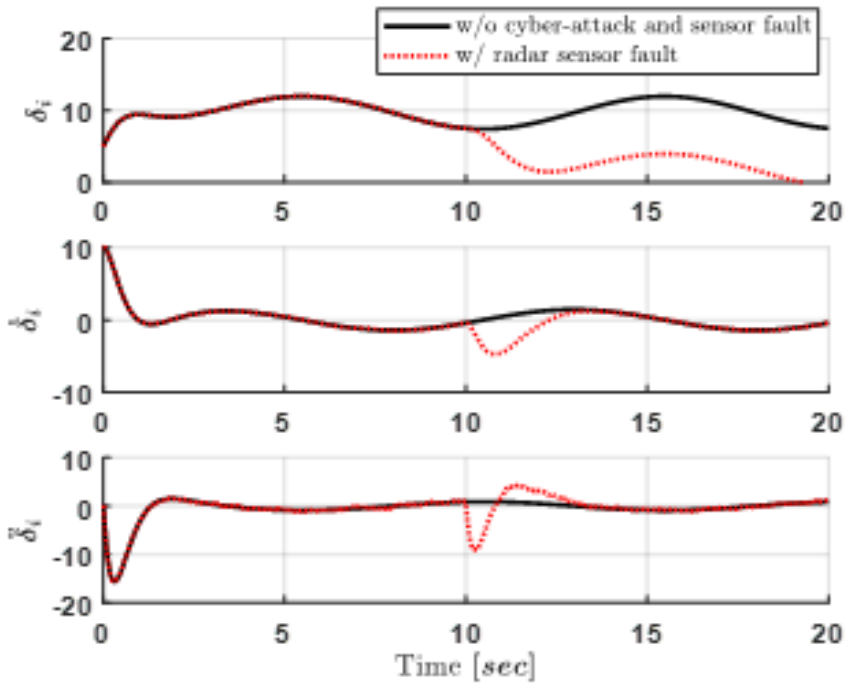

Figure 3.3: Behavior of SA-ACC system in the presence of the sensor fault in the velocity measurement channel of the radar.

sensor fault is generated as

$$f_r = \begin{cases} 8 & t \geq 10 \\ 0 & \text{otherwise} \end{cases} \tag{3.47}$$

Similar to the previous case, the following vehicle perceives an abrupt increase of the distance to the preceding vehicle. As shown in Figure 3.5, the following vehicle is controlled to increase the velocity of the vehicle to maintain the desired distance based on the wrong information. As a result, collision occurs at 19.33 seconds as shown in Figure 3.5. The results of the proposed observer are shown in Figure 3.6. As discussed, the sensor fault in the range measurement channel of the radar leads the proposed observer to provide non-zero value of $\hat{f}_s$. As shown in Figure 6, the sensor fault can be detected immediately at 10 seconds by monitoring $\hat{f}_s$. It is noted that this model-based approach has a limitation on detection of a sensor fault in range measurement channel of a radar. For example, the value of $\hat{f}_s$ will be very small if the range measurement channel has a fault such that ramp-type false signal with very small slope is added to the actual measurements.

3.5.2 Simulation Results with Cyber-Attacks

First, false data injection cyber-attack on the acceleration information is simulated, as shown in Figure 3.7 and 3.8. The inter-vehicle communication is attacked by injecting follow values

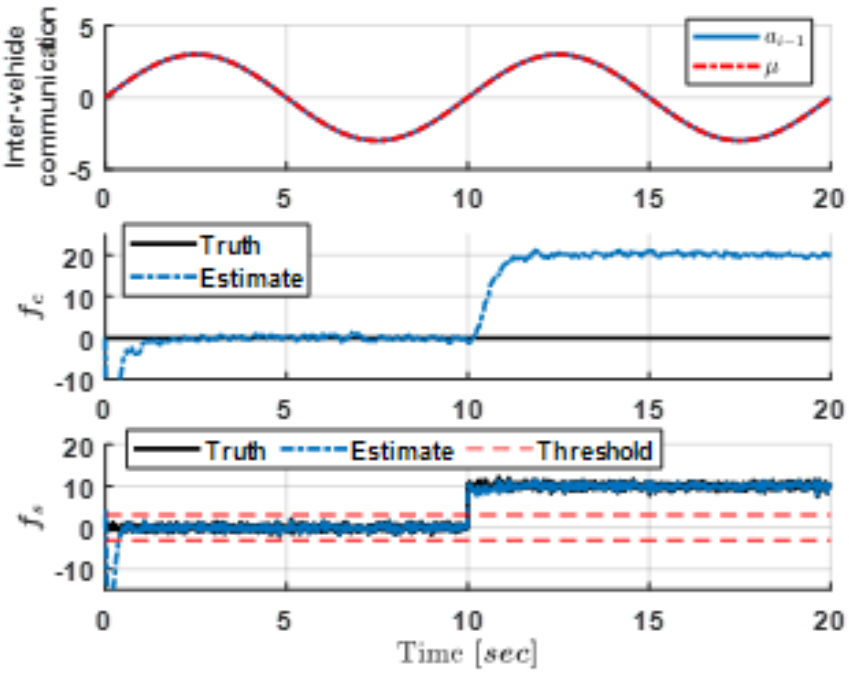

Figure 3.4: Acceleration of the preceding vehicle, cyber-attack estimation and sensor fault estimation in the presence of the sensor fault in the velocity measurement channel of the radar.

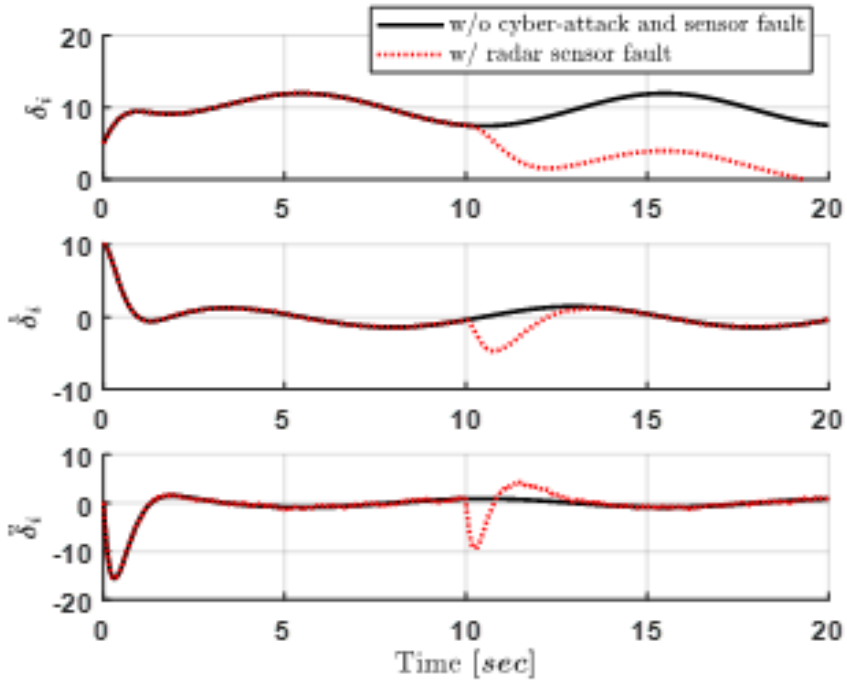

Figure 3.5: Behavior of SA-ACC system in the presence of the sensor fault in the range measurement channel of the radar.

on the acceleration information of the preceding vehicle:

$$f_a = \begin{cases} 3(t-10) & t \geq 10 \\ 0 & \text{otherwise} \end{cases} \tag{3.48}$$

Due to the cyber-attack, the following vehicle receives wrong information such that the preceding vehicle is accelerating as shown in Figure 3.7. This will likely result in a collision. Figure 3.8 shows the performance of the controller with the proposed observer. Once the cyber-attack is detected at 11.38 seconds in Figure 3.7, the system switches to the controller based on the proposed observer as shown in Figure 3.2 and maintains the desired distance with larger time gap while the cyber-attack exists as shown in Figure 3.8. Also, it is shown that the proposed observer estimates the injected false data f_a successfully.

Simulation studies also conducted to evaluate the SA-ACC system with the proposed observer in the presence of the DoS cyber-attack. DoS attack on the inter-vehicle communication channel is considered and it causes communication delay. We assume that the following vehicle receives the signal $\mu(t)$ as follows:

$$\mu(t) = \begin{cases} a_{i-1}(t) & t \leq t_1 \\ a_{i-1}(t_1) & t_1 \leq t \leq t_1 + \tau_d \\ a_{i-1}(t-\tau_d) & t \geq t_1 + \tau_d \end{cases} \tag{3.49}$$

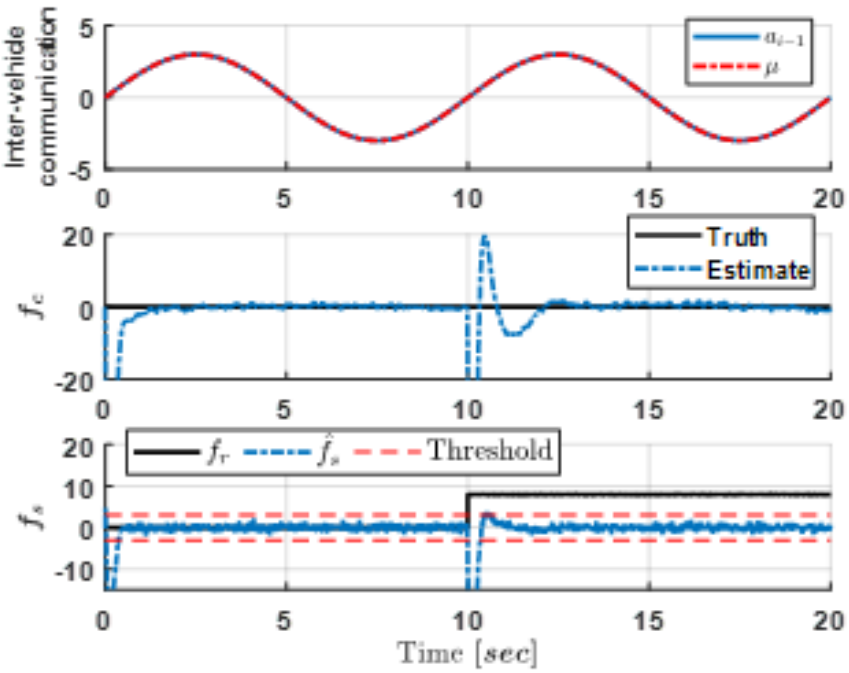

Figure 3.6: Acceleration of the preceding vehicle, cyber-attack estimation and sensor fault estimation in the presence of the sensor fault in the range measurement channel of the radar.

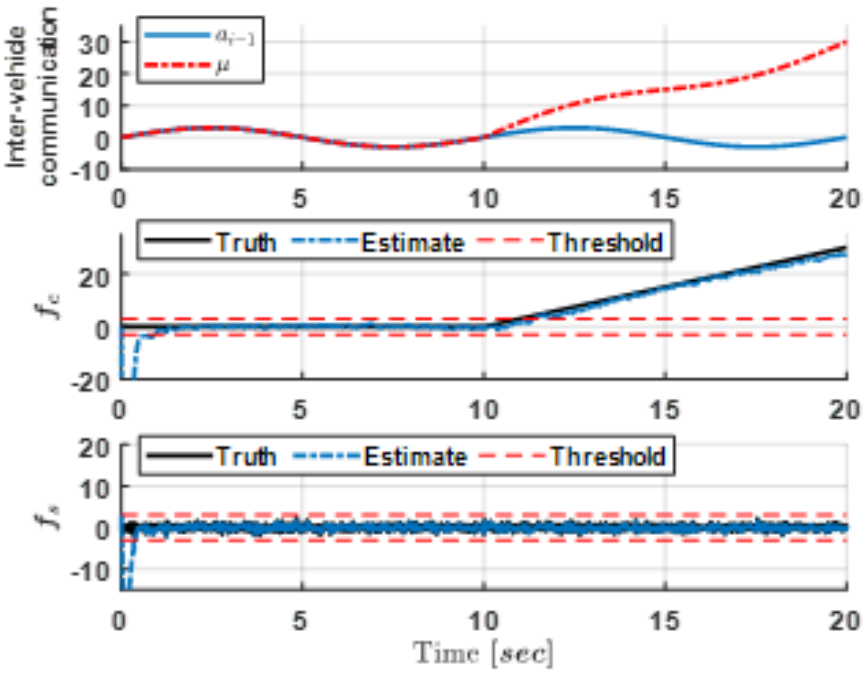

Figure 3.7: Acceleration of the preceding vehicle, cyber-attack estimation and sensor fault estimation in the presence of the false data injection cyber-attack on the communication channel.

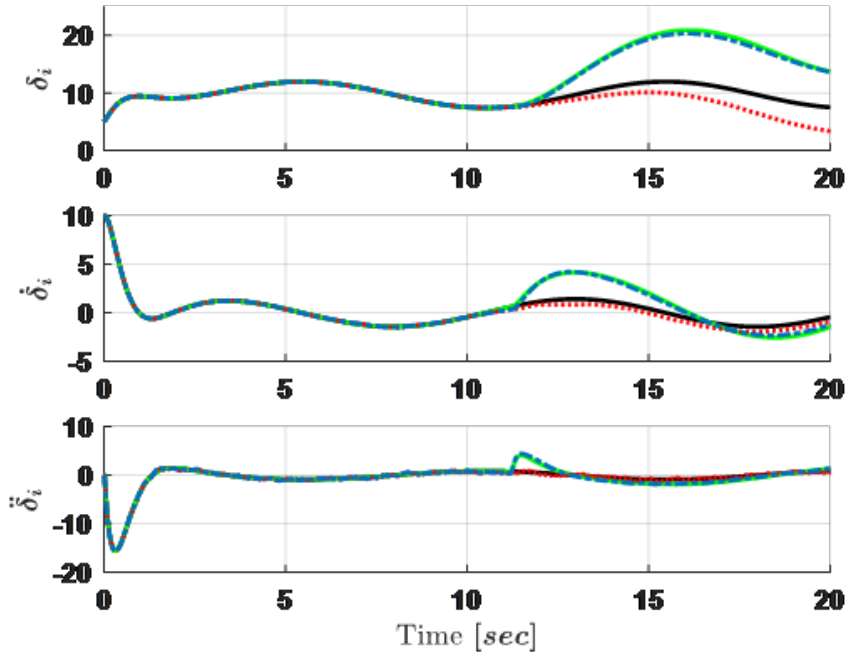

Figure 3.8: Behavior of SA-ACC system in the presence of the false data injection cyber-attack on the communication channel.

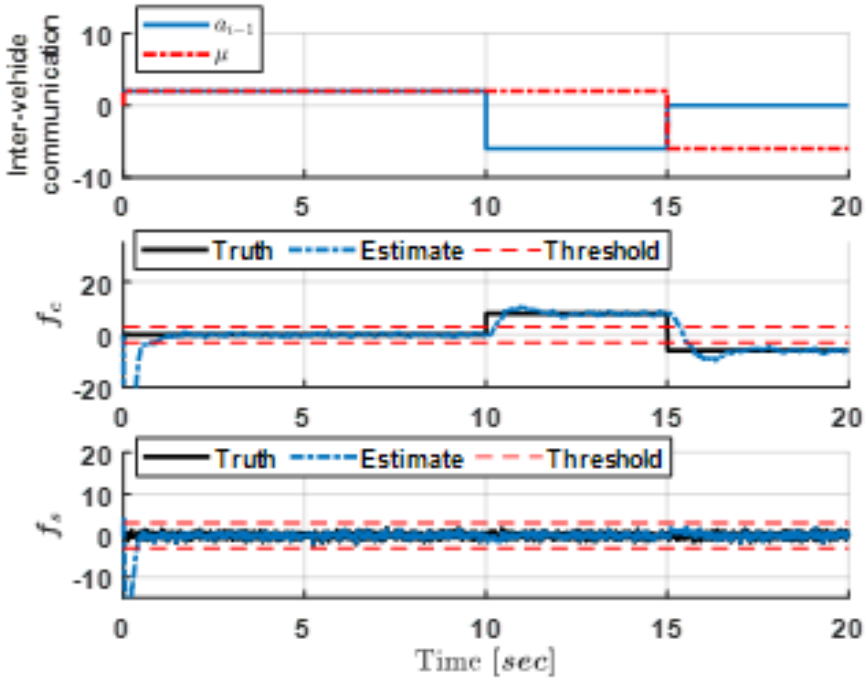

Figure 3.9: Acceleration of the preceding vehicle, cyber-attack estimation and sensor fault estimation in the presence of the denial of service cyber-attack on the communication channel.

where $t_1 = 10$ and $\tau_d = 5$. The true acceleration of the preceding vehicle and the delay signal due to DoS attack are shown in Figure 3.9. The preceding vehicle starts to decelerate at 10 seconds. However, because of the DoS cyber-attack, the following vehicle receives delay signal and cannot perceive the deceleration of the preceding vehicle. As a result, the SA-ACC system without using the proposed controller and observer cannot maintain desired distance between the preceding and following vehicles as shown in Figure 3.10. This may lead to fail to maintain of string stability. The proposed observer estimates false data due to the DoS cyber-attack successfully and detect the DoS attack at 10.26 seconds as shown in Figure 3.9. Furthermore, Figure 3.10 shows that the following vehicle maintains desired distance to the preceding vehicle even in the presence of DoS cyber-attack using the proposed observer-based controller.

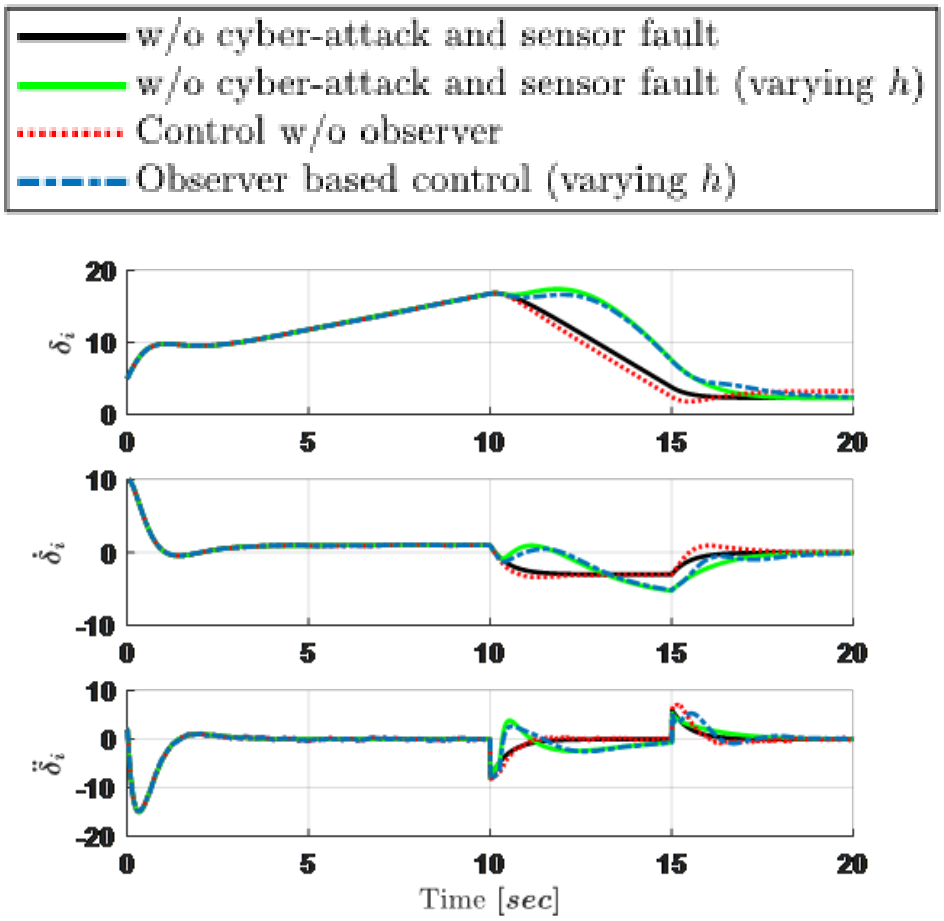

Figure 3.10: Behavior of SA-ACC system in the presence of the denial of service cyber-attack on the communication channel.

3.6 Conclusion

This chapter developed an observer for detection of cyber-attack on a communication channel which also simultaneously monitoring the health of the radar for a connected vehicle. A semi-autonomous adaptive cruise control (SA-ACC) vehicle was considered which used wireless communication with its immediately preceding vehicle in the same lane. The wireless connectivity enabled the vehicle to operate at small time-gap distances without creating string instability. However, the reliability of the wireless connectivity was critical for ensuring safe vehicle operation and a cyber-attack in this channel needed to be detected autonomously. The presence of two unknown inputs related to both sensor failure and cyber-attack seemingly posed a difficult estimation challenge.

The dynamic system was first represented in descriptor system form. Then an observer with estimation error dynamics decoupled from the cyber-attack signal was developed.

The performance of the observer was extensively evaluated in simulations. Simulation results showed that the estimation system was able to detect either a fault in the radar or a cyber-attack. Also, the proposed observer-based controller achieves resilient SA-ACC system under the cyber-attacks. The fundamental estimation algorithm developed herein can be extended in the future to enable cyber-attack detection in more complex connected vehicle architectures.

Chapter 4

Effects of cooperative adaptive cruise control on network traffic

4.1 Introduction

A major potential benefit from automated vehicles (AVs) is from increasing traffic flow through cooperative adaptive cruise control (CACC), in which vehicles use vehicle-to-vehicle communications to coordinate accelerations and decelerations. This coordination admits platoons of vehicles operating nearly at free flow speeds even at high densities. Microsimulation studies have consistently shown that CACC can improve road capacity (Kesting et al., 2010; Van Arem et al., 2006; Shladover et al., 2012). However, it is not known how such capacity improvements will affect traffic congestion. The well-known Braess (1968) paradox demonstrated that selfish route choice can completely offset network improvements, and Daganzo (1998) extended the result to more realistic traffic flow models.

The main impetus to research on the new inter-vehicle spacing policies comes from Rajamani (2011b) which discusses longitudinal control for vehicle platoons with adaptive cruise control (ACC). In this book, two controls were introduced: speed control is when there is no leading vehicles, AV should follow free flow speed; and car-following control is what this chapter focuses on: vehicles equipped with radar could access the moving information of preceding vehicles, which includes current location, velocity, and acceleration rate. Based on information from leading vehicles, the car-following vehicles could adjust their speed and acceleration to satisfy the predefined longitudinal requirement between two vehicles. Implementing longitudinal control can more precisely control the inter-vehicle spacing, reducing safety concerns. Comparing with conventional vehicles, AVs running on CACC road decreases the inter-vehicle spacing between every pair of adjacent vehicles, which will improve lane capacity.

In the current state of the literature, the inter-vehicle spacing was expressed by a linear equation of velocity. To reflect such improvement, Rajamani (2011b) proposed to use a quadratic equation of velocity to reflect the inter-vehicle spacing. As mentioned above, radar available to AVs could help decrease car-following distance, thereby increase traffic capacity. At that time, new relation between inter-vehicle spacing and velocity should come

up to capture the characteristic: with the same velocity, the inter-vehicle spacing needed for a conventional vehicles are longer than an AV.

The purpose of this chapter is to study the city-wide effects of a new CACC spacing policy. Fundamentally, the CACC spacing affects the flow-density relationship which defines the kinematic wave theory of traffic flow (Lighthill and Whitham, 1955; Richards, 1956). Due to the complexity of the partial differential equations comprising the kinematic wave theory, it is often solved numerically. The link transmission model (LTM) by Yperman et al. (2005) was chosen in this chapter because LTM does not discretize space within links, and LTM admits higher values of the congested wave speed without the numerical errors associated with the space discretization of the cell transmission model (Melson et al., 2018). However, the aforementioned proposition is from microscopic consideration, i.e. it is between every two adjacent vehicles.

Due to current technology availability, there will be a transition period when AVs and human vehicles (HV) coexist in the road network. This paper assumes that a set of lanes on specific freeway will be converted to AV-exclusive lanes. Although these lanes are not usable by HVs, they increase the network capacity when sufficient AVs are present to make use of them. Simulating LTM with fixed total demand and AV demand varying helps determine necessary AV market penetration to justify a set of AV dedicated lane. The results shows that he capacity improvements from CACC decrease traffic congestion on a freeway corridor. However, the reduced capacity available to HVs makes route choice a significant issue when considering the entire network, and overall congestion may not decrease.

4.2 Methodology

The purpose of this section is to develop an LTM modeling a quadratic vehicle spacing policy proposed by Rajamani (2011b). To do so, we must first find the flow-density relationship for this spacing policy, then adapt the existing LTM work to the new flow-density relationship. We start by developing the flow-density relationship for a linear vehicle spacing, which demonstrates the concepts and the differences, before moving to the quadratic vehicle spacing policy.

4.2.1 Linear vehicle spacing policy

For a linear vehicle spacing policy, the desired spacing between cars is:

$$S = L + hV \tag{4.1}$$

where S is the desired space between the head vehicle and following vehicle, L is the length of the preceding car, h is a chosen time-gap value, and V is velocity of the vehicles. Because the kinematic wave theory is a first-order model, we aim to find the spacing for constant speeds.

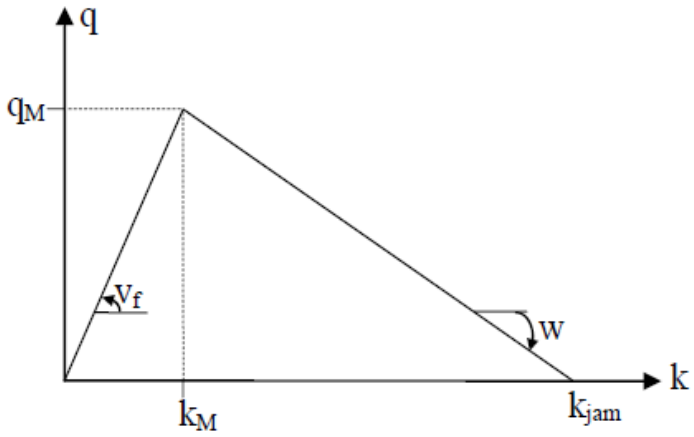

Figure 4.1: Fundamental diagram from a linear car-following spacing policy

The steady state density is vehicles per unit distance, which is the reciprocal of spacing:

$$\rho = \frac{1}{S} = \frac{1}{L + hV} \tag{4.2}$$

Getting the equation between velocity and density, inverse density to express velocity, we obtain:

$$V = \frac{1}{h}\left(\frac{1}{\rho} - L\right) \tag{4.3}$$

According to traffic flow theory, the flow q equals to the number of vehicles passed by observation point during time interval t, andthe density ρ is defined as number of vehicles per unit distance. Therefore, the flow equals to density times velocity, thus, the flow is:

$$q = \rho V = \frac{1}{h}\left(1 - \rho L\right) \tag{4.4}$$

The fundamental diagram of equation (4.4) defines the relation between traffic flow q and traffic density ρ when speed is restricted by car-following. Alternatively, speed is also restricted by the free flow speed of traffic. The flow-density relationship of equation (4.4) has a triangular shape as shown in Figure 4.1.

4.2.2 Quadratic vehicle spacing policy

Rajamani (2011b) proposed a quadratic vehicle spacing policy which admits closer spacing at certain speeds:

$$S = L + bV^2 \tag{4.5}$$

where b is a proportionality constant. Notice that the spacing always exceeds L to avoid a

collision. Following the same approach as in Section 4.2.1, we can obtain the relationship between flow and density. The steady state density with new desired spacing is

$$\rho = \frac{1}{L + bV^2} \tag{4.6}$$

To express density ρ using velocity V, we solve for V in equation (4.6) to obtain

$$V = \sqrt{\frac{1}{b}(\frac{1}{\rho} - L)} \tag{4.7}$$

Using the relationship $q = \rho V$, the flow-density relationship is obtained as

$$q = \rho V = \sqrt{\frac{1}{b}(\rho - L\rho^2)} \tag{4.8}$$

The flow-density relationship of equation (4.8) with $b = 0.1$ and $L = 5$ meter is depicted in Figure 4.2. Notice that this quadratic relationship constrains the flow, but it is possible for flow to remain positive at jam density. While this is counterintuitive, it is supported by experiments in the PATH program. Due to coordination of accelerations and decelerations, vehicles can maintain positive speeds at jam density. This is a major benefit of CACC in reducing the effects of queuing on traffic congestion.

4.2.3 Kinematic wave theory

Given the flow-density relationship, the objective is to solve the kinematic wave theory (Lighthill and Whitham, 1955; Richards, 1956). Although flow (q) and density (ρ) were used as static variables in the discussions of Sections 4.2.1 and 4.2.2, in reality flow and density varies over space (x) and time (t). Let $N(t, x)$ be the cumulative counts, i.e. the number of vehicles that have passed point x at or before time t. Then flow and density are defined as

$$\rho(t, x) = -\frac{\partial N(t, x)}{\partial x} \tag{4.9}$$

$$q(t, x) = \frac{\partial N(t, x)}{\partial t} \tag{4.10}$$

By the definition of a multivariable function,

$$\frac{\partial q(t, x)}{\partial x} = \frac{\partial^2 N(t, x)}{\partial t \partial x} = \frac{\partial^2 N(t, x)}{\partial x \partial t} = -\frac{\partial rho(t, x)}{\partial t} \tag{4.11}$$

which defines the flow conservation law. The second definition needed to solve the partial differential equation is the relationship between flow and density, $q(t, x) = f(\rho(t, x))$, where $f(\rho)$ is defined by equation (4.8).

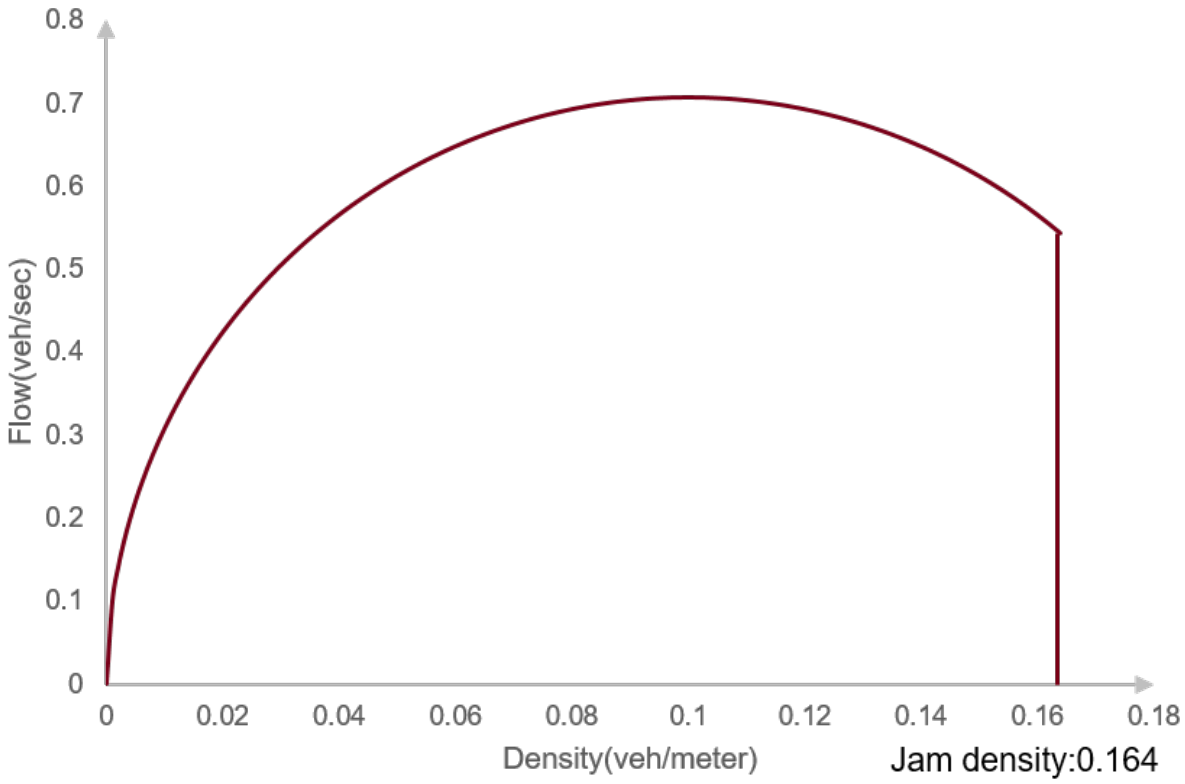

Figure 4.2: Fundamental diagram for quadratic vehicle spacing policy

4.2.4 Link transmission model

The kinematic wave theory is difficult to solve exactly, so most implementations have relied on numerical approximations. A commonly used approximation is the cell transmission model of Daganzo (1994); dag, which is a Godunov (1959) scheme that discretizes space and time into small intervals. Due to the Courant-Friedrich-Levy condition (Courant et al., 1967), large backwards shockwave speeds, such as those present in the flow-density relationship of equation (4.8), introduce numerical errors into the free flow propagation of vehicles. To avoid these numerical errors, we instead use LTM to model traffic (Yperman et al., 2005). LTM is based on Newell (1993)'s observation that the cumulative counts can be easily calculated along certain characteristic curves in the space-time domain.

To model city networks, each intersection or centroid is modeled as a *node* in the network, which are connected by *links* (road segments). Fundamentally, the objective in dynamic network loading over city networks is to simulate the movement of vehicles into and out of links. Define the sending flow of link i, $S_i(t)$, to be the maximum flow that could exit the downstream end of link i at time t. Similarly define the receiving flow $R_i(t)$ to be the maximum flow that could enter link i at time t. Consider two links i and j; the flow from link i to link j is constrained by $\min\left(S_i(t), R_j(t)\right)$. Of course, other intersection constraints (such as traffic signals) apply, but the essential idea is to choose the maximum flow subject to constraints on entering and exiting flows. In LTM, the sending and receiving flows are calculated by Yperman et al. (2005) as follows:

$$S_i(t) = \min\left(\left(N\left(x_i^0, t + \Delta t - \frac{\ell_i}{v_{\text{ffs},i}}\right) - N\left(x_i^L, t\right)\right), q_{\text{M},i}\Delta t\right) \tag{4.12}$$

$$R_j(t) = \min\left(N\left(x_i^L, t + \Delta t + \frac{\ell_j}{w_j}\right) + k_{\text{jam}}L_j - N\left(x_j^0, t\right), q_{\text{M},i}\Delta t\right) \tag{4.13}$$

where ℓ_i is the length, $v_{\text{ffs},i}$ is the free flow speed, $q_{\text{M},i}$ is the capacity, and Δt is the time step of the simulation.

The cumulative counts at the downstream boundary of an incoming link is calculated from the upstream link boundary using an accumulation of vehicle flows. Since LTM is defined for a piecewise-linear flow-density relationship, it is necessary to approximate equation (4.8) through a piecewise-linear function as shown in Figure 4.3. In Figure 4.3, from left to right, every segment has an equation, where x represents density changes and y represent corresponding flow changes. The parameter in front of density is the free flow speed when density varies in range.

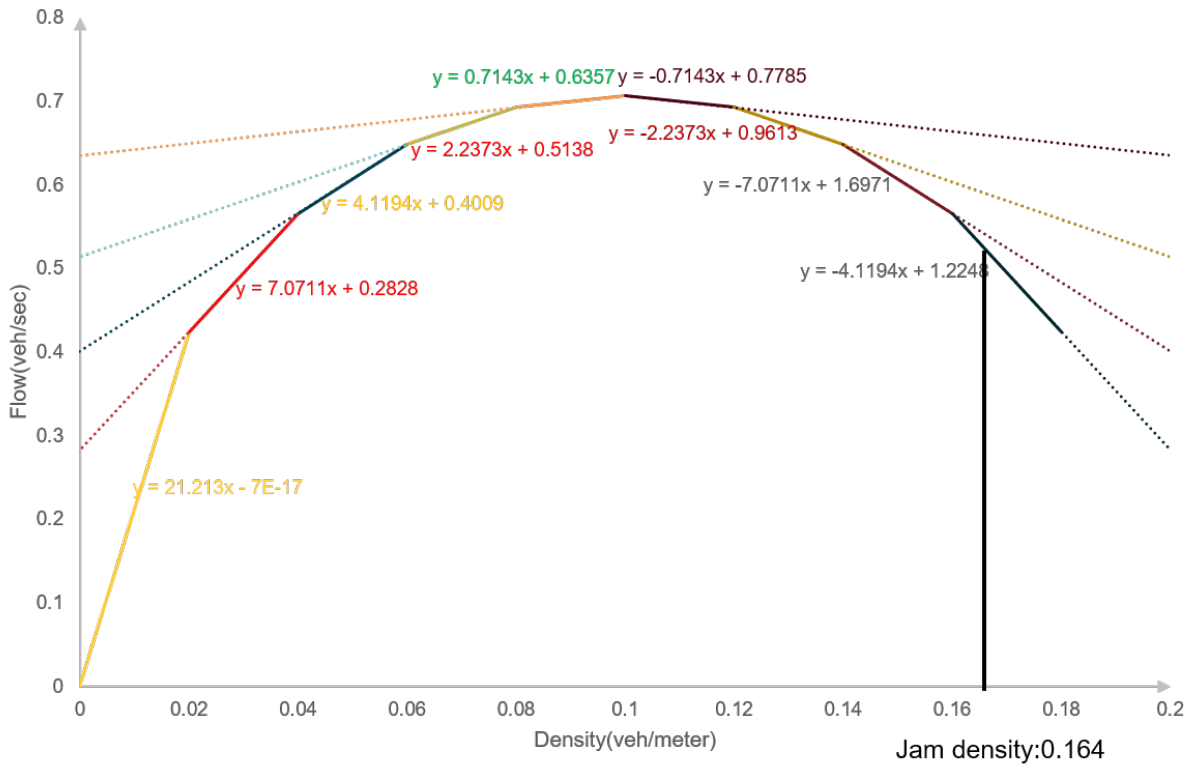

Figure 4.3: Piecewise-linear approximation to the flow-density relationship

4.3 Results

The methodology suggests that CACC should decrease inter-vehicle spacing and increase capacity. However, it is not clear how these capacity improvements are likely to affect traffic congestion. Two networks using calibrated data from the Austin, Texas region were used in the simulations. These networks were developed by city engineers and calibrated against observed link flows. The first network is a fairly simple freeway corridor, and the second network is the Round Rock network including both arterials and freeways. We conducted a variety of experiments on the combination of these two networks.

4.3.1 Austin I–35

The first network used is a fairly simple 28-mile freeway corridor of I-35 near Austin, Texas, shown in Figure 4.4. The purpose of this network is to evaluate the capacity improvements in a straightforward setting without compounding factors such as route choice. Since this network is a freeway corridor, vehicles merge into and get off the freeway without route choice. For this network, we chose a demand of 128,051 over 4 hours, which creates sufficient congestion to test the capacity improvements of CACC while avoiding unrealistic congestion that creates gridlock.

Two comparison scenarios were implemented to test CACC effect: first, running the base scenario with 100% HV demand, i.e. all demand are conventional passengers in personal vehicles, and all vehicles behave normally. The second scenario involves converting all conventional lanes to CACC lanes, and all vehicles are assumed to be automated. The resulting travel times are shown in 4.1. (Although the freeway corridor is 28 miles long, most trips do not use the entire corridor). Table 4.1 shows that at 100% autonomous vehicle market rate, implementing CACC reduced travel times by 64.9%, from 23953 to 8400, compared with the base scenario. The reduction in travel times is due to the increase in capacity as well as the increases in flow past the critical density, both of which result in greater overall flow on the freeway.

4.3.2 Round Rock, Texas

After demonstrating that CACC platooning with high AV demand indeed mitigates system congestion, we conduct simulations on a more complete network based on the city of Round Rock, Texas as shown in Figure 4.5. This network has 2744 nodes (716 zones) and 4236 links. In this network, 1 lane on each of the freeway corridors (shown in green in Figure 4.5)

Table 4.1: Comparison result of Austin I–35 corridor

	0% AVs	100% AVs
Total Demand	128051	128051
TSTT	23953 hours	8400 hours
Average travel time	11.22 mins	3.94 mins

Figure 4.4: Freeway corridor of Austin I–35

was converted to CACC. (Each of these freeway links had at least 2 lanes). This provided a significant increase in capacity for AVs while also preserving connectivity for HVs. Due to the vehicle connectivity required for CACC, we assumed that AVs and HVs have identical car-following behavior on shared lanes. AVs can only use the quadratic vehicle spacing policy on AV-exclusive lanes.

The major difference between this network and I–35 is the presence of multiple routes between most origin-destination pairs. Consequently, route choice is a component of this model. Following the principal of Wardrop (1952), we assume that users choose routes to minimize their travel times. As the route choice affects the traffic congestion on individual links, the travel times and route choices have a mutual feedback process. We seek to find dynamic user equilibrium, in which no user can reduce their travel times (at their time of departure) by changing routes. This is known as the dynamic traffic assignment problem (Chiu et al., 2011). The selfish route choice creates the potential for the Braess (1968) paradox, in which improvements in network capacity paradoxically cause increases in traffic congestion. To solve dynamic traffic assignment, we used the method of successive averages (Levin et al., 2015).

Multiple scenarios of AV market penetration were considered, and dynamic traffic assignment was solved separately for each scenario. The base scenario considers 100% HVs without any CACC lanes. The other experiments converted one freeway lane to CACC on the freeway links shown. Each of these links had at least two lanes to preserve connectivity for HVs. The conventional lane and AV dedicated lane are modeled as parallel links; AVs can choose to use either one based on travel times. This conversion reduced the freeway capacity for HVs, but AVs can use CACC lane which creates a net increase in network capacity.

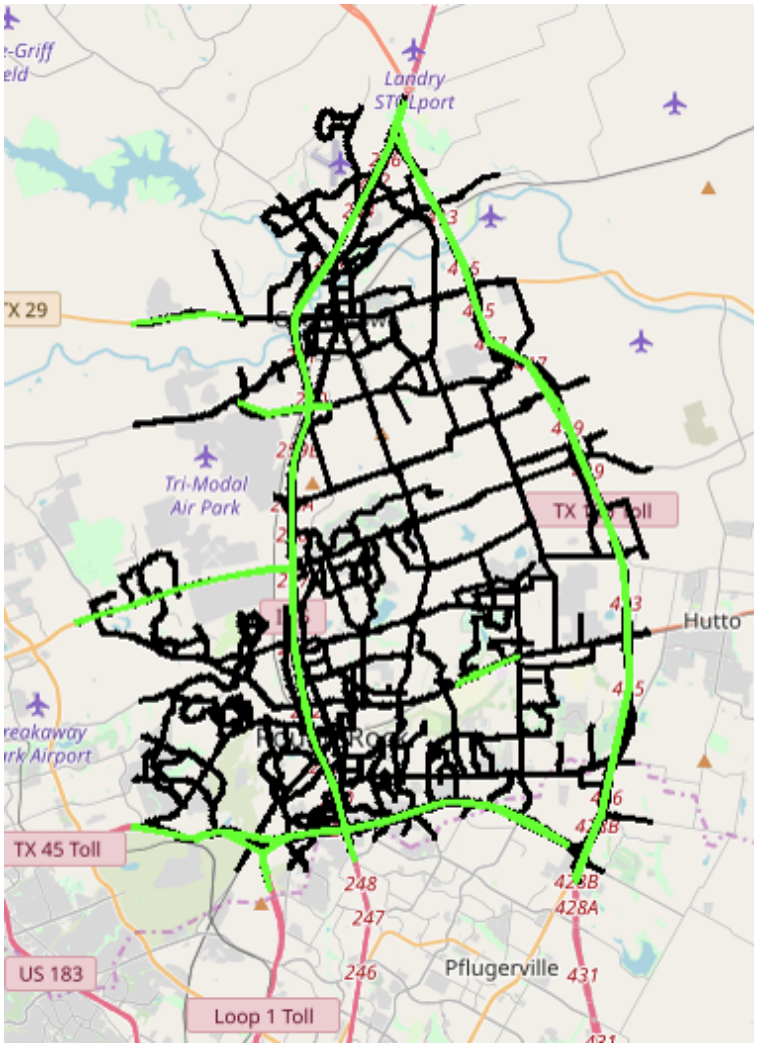

Figure 4.5: Round Rock, Texas network

We studied a variety of AV market penetration scenarios. We fixed the total demand as 156, 664 over 7 hours, which includes significant congestion. The experimental scenarios involved increasing AV market penetration from 0% to 100%. Figure 4.6 shows the total system travel time results. The maroon solid line represent the base scenario with no AV lanes, so no changes in travel times are observed. The yellow dash line reflects how TSTT change as the AV market penetration increases. Figure 4.6 shows that as AV demand increases, TSTT decrease gradually. However, it is always above the baseline which has no AV demand at all.

To investigate further, we compared the average travel times specifically for AVs and HVs in Figure 4.7. As expected, AV travel time is significantly less than HV travel time because AVs have access to higher-capacity freeway lanes, which should be less congested. However, AVs still experienced higher average travel times than the base scenario. Meanwhile, HVs were significantly affected by congestion, experiencing high increases in average travel times

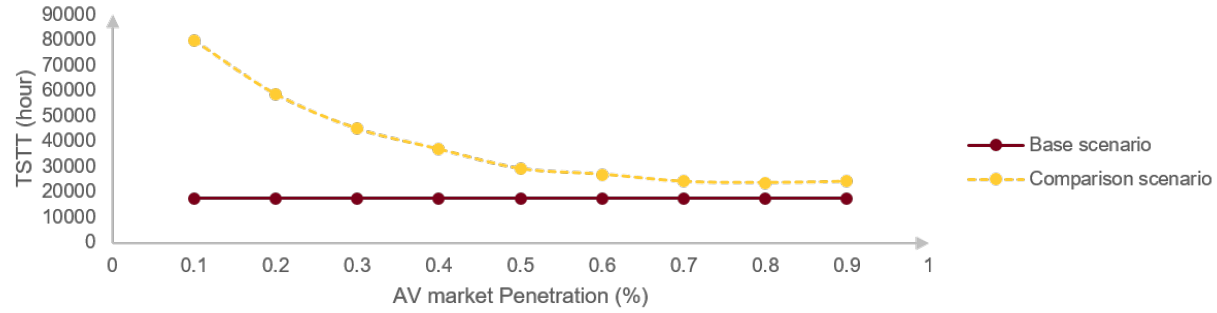

Figure 4.6: TSTT versus AV market penetration

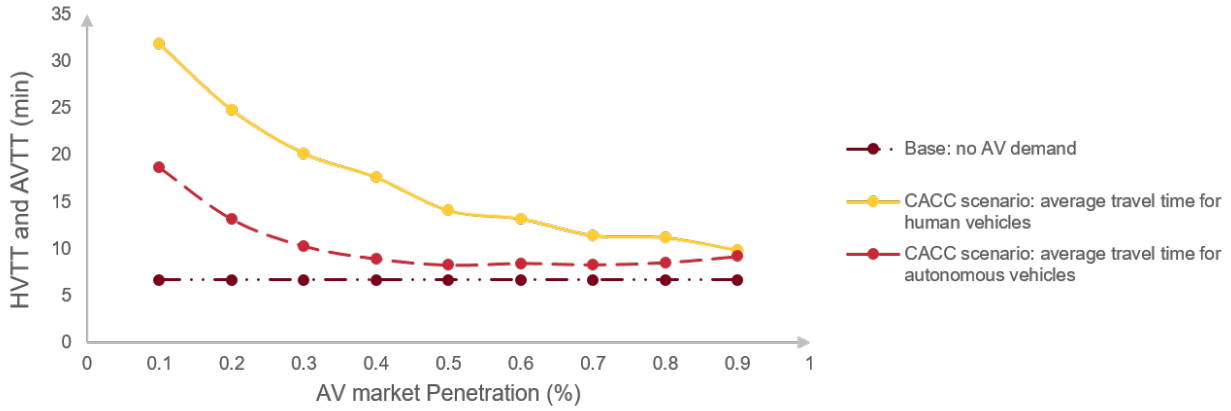

Figure 4.7: HVTT and AVTT versus AV market penetration

especially at low AV market penetrations. Some of this result is undoubtedly due to capacity reductions on freeways, resulting in greater congestion on the limited lanes available to HVs. However, AVs also experienced higher travel times from the introduction of CACC lanes, which indicates that the network structure is also to blame. Consider the network topology shown in Figure 4.5. As is typical of most networks, freeway links are connected to major destinations through arterial roads. Most vehicle trips must traverse arterial roads before reaching a freeway. Although AVs enjoyed greater capacity and lower congestion on freeways, they first had to pass through arterial links to enter the freeway. Due to the reduced freeway capacity available to HVs, those HVs were more inclined to take arterial roads, resulting in greater congestion there. Consequently, AVs experienced higher travel times due to the higher congestion on shared arterial roads.

4.4 Conclusions

Although CACC has largely been developed as a novel spacing control for individual vehicles, this chapter studied its effects at the city network level. First, the flow-density relationship for a new quadratic spacing policy from Rajamani (2011b) was derived. As expected, the

flow-density relationship for CACC includes a higher capacity as well as positive flow at jam density. Consequently, the limitations on flow are greatly lessened, which was expected to significantly improve freeway traffic flow. We defined a corresponding kinematic wave theory, and used the link transmission model (Yperman et al., 2005) to numerically approximate it.

This numerical simulation method was incorporated into dynamic network loading to study the effects on traffic congestion on calibrated city networks. The first experiment on the 28-mile I–35 freeway corridor showed significant reductions in average travel times which correspond to the capacity improvements from CACC. However, results on the Round Rock, Texas network showed that route choice could confound the capacity improvements from CACC. Even at higher AV market penetrations, greater use of arterial roads by HVs resulted in higher travel times for both AVs and HVs. Consequently, we conclude that the deployment of CACC lanes requires greater consideration. It is entirely possible to increase congestion due to route choice changes induced by converting freeway lanes to platooning lanes. Transportation engineers should use dynamic traffic assignment planning models and network design tools to determine if and when CACC lanes can be deployed effectively. In future work, we intend to evaluate the effects of CACC lanes on other city networks, and study the network design problem of when to deploy CACC lanes.

Chapter 5

Conclusions and Future Work

This seed project brought together two separate, multidisciplinary research groups of PIs Drs. Levin and Rajamani to study sensor-related technology for estimating the traffic state and improving vehicle car-following behavior. Three studies were conducted which should lead to peer-reviewed conference or journal publications that will support future proposals. First, the project team studied the problem of estimating vehicle trajectories and the evolution of flow and density over space and time using basic safety messages from connected vehicles. A novel Kalman filtering method, using two Kalman filters to estimate the fundamental diagram parameters and the densities of discrete spatial intervals, was developed and tested in simulation. Since the safety of vehicle controls that relies on inter-vehicle communications is vulnerable to cyberattacks, the project team studied methods of detecting and responding to faulty or malicious data transmitted by vehicles for cooperative adaptive cruise control. Finally, the project team studied the effects of cooperative adaptive cruise control at a city network level by converting the car-following behavior into a new fundamental diagram, creating a link transmission model to approximate the resulting kinematic wave theory, and solving dynamic traffic assignment. Results on the Round Rock network indicate that route choice played a significant role in the benefits of platooning lanes. Route choice changes caused by reserving lanes for automated vehicles can create congestion despite increases in network capacity.

The developing technology of connected and automated vehicles is rapidly emerging, and has created many scientific questions of how they could and should affect traffic. Although novel traffic operations for fully automated vehicles (such as signal-free intersection control) have received extensive attention in the literature, of more immediate importance is practical use of the partial connectivity and automation that is already available to consumers on some new vehicles. The PIs believe that using connected vehicle broadcasted data is an especially ripe area for future research with near-term practical implications. Using the papers developed from this project as preliminary work, the PIs are currently drafting an NSF proposal. Due to the novelty of the problems, significant scientific and analytical questions remain. Due to the lack of experimental demonstrators, the PIs believe that NSF is well-suited for funding this type of research.

Future studies anticipated as a result of this seed project include:

- Detection of malicious or erroneous connected vehicle data within traffic state estimation.
- Use of sensors (such as loop detectors) in combination with limited numbers of connected vehicles to improve the accuracy of traffic state knowledge in the near future.
- Network design for locating platooning lanes, considering dynamic user equilibrium route choice as a subproblem.

References

The cell transmission model, part ii.

Bakhshande, F. and Söffker, D. (2015). Proportional-integral-observer: A brief survey with special attention to the actual methods using acc benchmark. *IFAC-PapersOnLine*, 48(1):532–537.

Biron, Z. A., Dey, S., and Pisu, P. (2018). Real-time detection and estimation of denial of service attack in connected vehicle systems. *IEEE Transactions on Intelligent Transportation Systems*, (99):1–10.

Boukhari, M., Chaibet, A., Boukhnifer, M., and Glaser, S. (2018). Proprioceptive sensors fault tolerant control strategy for an autonomous vehicle. *Sensors*, 18(6):1893.

Braess, P.-D. (1968). Über ein paradoxon aus der verkehrsplanung. *Unternehmensforschung*, 12(1):258–268.

Chiu, Y.-C., Bottom, J., Mahut, M., Paz, A., Balakrishna, R., Waller, T., and Hicks, J. (2011). Dynamic traffic assignment: A primer. *Transportation Research E-Circular*, (E-C153).

Courant, R., Friedrichs, K., and Lewy, H. (1967). On the partial difference equations of mathematical physics. *IBM Journal of Research and Development*, 11(2):215–234.

Daganzo, C. F. (1994). The cell transmission model: A dynamic representation of highway traffic consistent with the hydrodynamic theory. *Transportation Research Part B: Methodological*, 28(4):269–287.

Daganzo, C. F. (1998). Queue spillovers in transportation networks with a route choice. *Transportation Science*, 32(1):3–11.

Godunov, S. K. (1959). A difference method for numerical calculation of discontinuous solutions of the equations of hydrodynamics. *Matematicheskii Sbornik*, 89(3):271–306.

Hellinga, B., Izadpanah, P., Takada, H., and Fu, L. (2008). Decomposing travel times measured by probe-based traffic monitoring systems to individual road segments. *Transportation Research Part C: Emerging Technologies*, 16(6):768–782.

Herring, R., Hofleitner, A., Abbeel, P., and Bayen, A. (2010). Estimating arterial traffic conditions using sparse probe data. In *Intelligent Transportation Systems (ITSC), 2010 13th International IEEE Conference on*, pages 929–936. IEEE.

Jagielski, M., Jones, N., Lin, C.-W., Nita-Rotaru, C., and Shiraishi, S. (2018). Threat detection for collaborative adaptive cruise control in connected cars. In *Proceedings of the 11th ACM Conference on Security & Privacy in Wireless and Mobile Networks*, pages 184–189. ACM.

Kalman, R. E. (1960). A new approach to linear filtering and prediction problems. *Journal of Basic Engineering*, 82(1):35–45.

Kesting, A., Treiber, M., and Helbing, D. (2010). Enhanced intelligent driver model to access the impact of driving strategies on traffic capacity. *Philosophical Transactions of the Royal Society of London A: Mathematical, Physical and Engineering Sciences*, 368(1928):4585–4605.

Khalil, H. K. and Grizzle, J. W. (2002). *Nonlinear systems*, volume 3. Prentice hall Upper Saddle River, NJ.

Lang, D., Stanger, T., and del Re, L. (2013). Opportunities on fuel economy utilizing v2v based drive systems. Technical report, SAE Technical Paper.

Levin, M. W., Pool, M., Owens, T., Juri, N. R., and Waller, S. T. (2015). Improving the convergence of simulation-based dynamic traffic assignment methodologies. *Networks and Spatial Economics*, 15(3):655–676.

Li, H., Remias, S. M., Day, C. M., Mekker, M. M., Sturdevant, J. R., and Bullock, D. M. (2015). Shock wave boundary identification using cloud-based probe data. *Transportation Research Record: Journal of the Transportation Research Board*, (2526):51–60.

Lighthill, M. J. and Whitham, G. B. (1955). On kinematic waves. ii. a theory of traffic flow on long crowded roads. In *Proceedings of the Royal Society of London A: Mathematical, Physical and Engineering Sciences*, volume 229, pages 317–345. The Royal Society.

Melson, C. L., Levin, M. W., Hammit, B. E., and Boyles, S. D. (2018). Dynamic traffic assignment of cooperative adaptive cruise control. *Transportation Research Part C: Emerging Technologies*, 90:114–133.

Newell, G. F. (1993). A simplified theory of kinematic waves in highway traffic, part I: General theory. *Transportation Research Part B: Methodological*, 27(4):281–287.

Oh, K., Park, S., Lee, J., and Yi, K. (2018). Functional perspective-based probabilistic fault detection and diagnostic algorithm for autonomous vehicle using longitudinal kinematic model. *Microsystem Technologies*, 24(11):4527–4537.

Parkinson, S., Ward, P., Wilson, K., and Miller, J. (2017). Cyber threats facing autonomous and connected vehicles: Future challenges. *IEEE Transactions on Intelligent Transportation Systems*, 18(11):2898–2915.

Petit, J. and Shladover, S. E. (2014). Potential cyberattacks on automated vehicles. *IEEE Transactions on Intelligent Transportation Systems*, 16(2):546–556.

Phanomchoeng, G. and Rajamani, R. (2013). Real-time estimation of rollover index for tripped rollovers with a novel unknown input nonlinear observer. *IEEE/ASME Transactions on Mechatronics*, 19(2):743–754.

Phanomchoeng, G., Zemouche, A., Jeon, W., Rajamani, R., and Mazenc, F. (2018). An h_∞ observer for descriptor nonlinear systems with nonlinear output equations. In *American Control Conference, ACC 2018*.

Rahmani, M., Jenelius, E., and Koutsopoulos, H. N. (2015). Non-parametric estimation of route travel time distributions from low-frequency floating car data. *Transportation Research Part C: Emerging Technologies*, 58:343–362.

Rajamani, R. (2011a). *Vehicle dynamics and control*. Springer Science & Business Media.

Rajamani, R. (2011b). *Vehicle dynamics and control*. Springer Science & Business Media.

Rajamani, R. and Zhu, C. (2002). Semi-autonomous adaptive cruise control systems. *IEEE Transactions on Vehicular Technology*, 51(5):1186–1192.

Richards, P. I. (1956). Shock waves on the highway. *Operations Research*, 4(1):42–51.

Rouphail, N. M., Kim, S., and Aghdashi, S. (2017). Application of high-resolution vehicle data for free-flow speed estimation. *Transportation Research Record: Journal of the Transportation Research Board*, (2615):105–112.

Shladover, S., Su, D., and Lu, X.-Y. (2012). Impacts of cooperative adaptive cruise control on freeway traffic flow. *Transportation Research Record: Journal of the Transportation Research Board*, (2324):63–70.

Siegel, J. E., Erb, D. C., and Sarma, S. E. (2017). A survey of the connected vehicle landscape-architectures, enabling technologies, applications, and development areas. *IEEE Transactions on Intelligent Transportation Systems*, 19(8):2391–2406.

Sun, X., Muñoz, L., and Horowitz, R. (2003). Highway traffic state estimation using improved mixture kalman filters for effective ramp metering control. In *42nd IEEE International Conference on Decision and Control (IEEE Cat. No. 03CH37475)*, volume 6, pages 6333–6338. IEEE.

Van Arem, B., Van Driel, C. J., and Visser, R. (2006). The impact of cooperative adaptive cruise control on traffic-flow characteristics. *IEEE Transactions on Intelligent Transportation Systems*, 7(4):429–436.

van der Heijden, R., Lukaseder, T., and Kargl, F. (2017). Analyzing attacks on cooperative adaptive cruise control. In *2017 IEEE Vehicular Networking Conference (VNC)*, pages 45–52.

Wang, C., Ran, B., Yang, H., Zhang, J., and Qu, X. (2018). A novel approach to estimate freeway traffic state: Parallel computing and improved kalman filter. *IEEE Intelligent Transportation Systems Magazine*, 10(2):180–193.

Wang, Y. and Papageorgiou, M. (2005). Real-time freeway traffic state estimation based on extended kalman filter: a general approach. *Transportation Research Part B: Methodological*, 39(2):141–167.

Wang, Y., Papageorgiou, M., and Messmer, A. (2008). Real-time freeway traffic state estimation based on extended kalman filter: Adaptive capabilities and real data testing. *Transportation Research Part A: Policy and Practice*, 42(10):1340–1358.

Wang, Z., Lu, M., Yuan, X., Zhang, J., and Van De Wetering, H. (2013). Visual traffic jam analysis based on trajectory data. *IEEE Transactions on Visualization and Computer Graphics*, 19(12):2159–2168.

Wardrop, J. G. (1952). Road paper. some theoretical aspects of road traffic research. In *ICE Proceedings: Engineering Divisions*, volume 1, pages 325–362. Thomas Telford.

Work, D. B., Tossavainen, O.-P., Blandin, S., Bayen, A. M., Iwuchukwu, T., and Tracton, K. (2008). An ensemble Kalman filtering approach to highway traffic estimation using gps enabled mobile devices. In *Decision and Control, 2008. CDC 2008. 47th IEEE Conference on*, pages 5062–5068. IEEE.

Work, D. B., Tossavainen, O.-P., Jacobson, Q., and Bayen, A. M. (2009). Lagrangian sensing: traffic estimation with mobile devices. In *American Control Conference, 2009. ACC'09.*, pages 1536–1543. IEEE.

Yao, B., Chen, C., Cao, Q., Jin, L., Zhang, M., Zhu, H., and Yu, B. (2017). Short-term traffic speed prediction for an urban corridor. *Computer-Aided Civil and Infrastructure Engineering*, 32(2):154–169.

Yperman, I., Logghe, S., and Immers, B. (2005). The link transmission model: An efficient implementation of the kinematic wave theory in traffic networks. In *Proceedings of the 10th EWGT Meeting, Poznan, Poland*.

Zhan, X., Zheng, Y., Yi, X., and Ukkusuri, S. V. (2017). Citywide traffic volume estimation using trajectory data. *IEEE Transactions on Knowledge & Data Engineering*, (2):272–285.

Zheng, F. and Van Zuylen, H. (2013). Urban link travel time estimation based on sparse probe vehicle data. *Transportation Research Part C: Emerging Technologies*, 31:145–157.

Zhu, T., Kong, X., and Lv, W. (2009). Large-scale travel time prediction for urban arterial roads based on Kalman filter. In *2009 International Conference on Computational Intelligence and Software Engineering*, pages 1–5.